

Article

# Process Parameter Optimization of 2507 Super Duplex Stainless Steel Additively Manufactured by the Laser Powder Bed Fusion Technique

Ali Mulhi <sup>1</sup>, Shirin Dehgahi <sup>1</sup>, Prashant Waghmare <sup>2</sup>  and Ahmed J. Qureshi <sup>1,\*</sup>

<sup>1</sup> Additive Design and Manufacturing Systems Laboratory, University of Alberta, Edmonton, AB T6G 2R3, Canada

<sup>2</sup> Interfacial Science and Surface Engineering Lab., University of Alberta, Edmonton, AB T6G 2R3, Canada

\* Correspondence: [ajqureshi@ualberta.ca](mailto:ajqureshi@ualberta.ca); Tel.: +1-780-492-2378

**Abstract:** Laser powder bed fusion is an attractive technology for producing high-strength stainless steel alloys. Among the stainless steels, 2507 super duplex stainless steel (2507 SDSS) is known for its excellent combination of corrosion resistance and high strength. Although there are some studies that aimed at optimizing the laser powder bed fusion (LPBF) printing parameters to print highly dense 2507 SDSS parts; However, a full optimization study is not reported yet. This study aims at optimizing the printing parameters for 2507 SDSS, namely: laser power, scan speed, and hatch distance. The response surface methodology was used in generating a detailed design of experiment to investigate the different pore formation types over a wide energy density range (22.22–428.87 J/mm<sup>3</sup>), examine the effects of each process parameter and their interactions on the resulting porosity, and identify an optimized parameter set for producing highly dense parts. Different process parameters showed different pore formation mechanisms, with lack-of-fusion, metallurgical or gas, and keyhole regimes being the most prevalent pore types identified. The lack-of-fusion pores are observed to decrease significantly with increasing the energy density at low values. However, a gradual increase in the keyhole pores was observed at higher energy densities. An optimal energy density process window from 68.24 to 126.67 J/mm<sup>3</sup> is identified for manufacturing highly dense ( $\geq 99.6\%$ ) 2507 SDSS parts. Furthermore, an optimized printing parameter set at a laser power of 217.4 W, a scan speed of 1735.7 mm/s, and a hatch distance of 51.3  $\mu\text{m}$  was identified, which was able to produce samples with 99.961% relative density. Using the optimized parameter set, the as-built 2507 SDSS sample had a ferrite phase fraction of 89.3% with a yield and ultimate tensile strength of  $1115.4 \pm 120.7$  MPa and  $1256.7 \pm 181.9$  MPa, respectively.

**Keywords:** laser powder bed fusion (lpbf); 2507 super duplex stainless steel; printing process optimization; response surface methodology; microcomputed X-ray tomography



**Citation:** Mulhi, A.; Dehgahi, S.; Waghmare, P.; Qureshi, A.J. Process Parameter Optimization of 2507 Super Duplex Stainless Steel Additively Manufactured by the Laser Powder Bed Fusion Technique. *Metals* **2023**, *13*, 725. <https://doi.org/10.3390/met13040725>

Academic Editors: Behzad Fotovvati, Praveen Sathiyamoorthi and Gangaraju Manogna Karthik

Received: 18 February 2023

Revised: 13 March 2023

Accepted: 22 March 2023

Published: 7 April 2023



**Copyright:** © 2023 by the authors. Licensee MDPI, Basel, Switzerland. This article is an open access article distributed under the terms and conditions of the Creative Commons Attribution (CC BY) license (<https://creativecommons.org/licenses/by/4.0/>).

## 1. Introduction

Laser powder bed fusion (LPBF) is an additive manufacturing technique in which a laser energy source is used to melt successive powder layers generating three-dimensional parts based on computer-aided design (CAD) models [1]—a review of the technology has been reported in [2]. The advances in the technology end-use parts with enhanced material quality, density, and consequently improved mechanical properties have grown significantly in recent years. Moreover, due to field applications such as medical, oil, and aerospace, which require manufactured parts with high quality and reliability, the LPBF process optimization has been significantly investigated with success [3–6].

It has been reported that more than 100 parameters play role in the LPBF manufactured part quality [7–9]. However, it was found that the laser power ( $p$ ), scan speed ( $v$ ), hatch distance ( $h$ ), and layer thickness ( $t$ ) had the most prominent effect on the microstructure and mechanical properties of the printed parts [10]. The term volumetric energy density ( $E_D$ ) is

a factor that is commonly used to guide the LPBF printing process optimization [11], and can be calculated using Equation (1). This factor relates the different printing parameters together and indicates the amount of energy input to the powder material during the printing process.

$$E_D = \frac{p}{v \cdot h \cdot t} \quad (1)$$

LPBF technology has some advantages over conventional manufacturing methods, including design freedom, manufacturing of complex part designs, reduced part weight, production of nearly net-shaped parts, and decreasing waste material [12]. However, one major drawback of LPBF is the formation of pores (i.e., porosity) in the final printed parts, which can lead to compromised mechanical properties [13]. Several pore formation mechanisms have been reported in LPBF, with keyhole mode pores, metallurgical or gas pores, and lack-of-fusion pores being the three most prevalent types associated with the printing process parameters [14]. Keyhole mode pores form when the energy density ( $E_D$ ) is too high (i.e., due to high laser power, slow scan speed, or low hatch distance), causing rapid metal vaporization at the melt pool surface resulting in a metal vapor recoil pressure that pushes the melt pool surface downwards and closes in on itself creating a cavity filled with metal vapor and shielding gas, referred to as keyhole or vapor depression [15]. The resulting keyhole pores are usually rounded but not completely spherical. Lack-of-fusion pores form when the energy density is too low, causing an insufficient melting of the powder, which results in large pores with irregular shapes and sizes, and often containing unmelted trapped powder particles [16]. Metallurgical or gas pores are mostly spherical and relatively small in size and are observed in the intermediate regime of energy density. These pores form due to the shielding gas entrapment, porosity of feedstock powder particles, or alloy vapors within the molten pool [2].

There are some studies that have used high-resolution microcomputed X-ray tomography ( $\mu$ CT) imaging to investigate the keyhole and lack-of-fusion pores under a range of identified printing process parameters [17,18]. As such,  $\mu$ CT imaging is adopted in this study for the porosity characterization and quantification analysis. The use of laboratory X-ray tomography for an in-depth examination of additively manufactured parts, along with several efforts to image various porosity types is reviewed in [19]. Moreover, the use of real-time fast microcomputed X-ray imaging has successfully been used in porosity formation analysis. This includes studies on the keyhole pore formation and particle spatter in melt pool dynamics [20], the dynamics of defects and melt pool showing the mechanisms of pore formation [21], and the keyhole vapor depression formation threshold [22], amongst others. Furthermore, a distinct reported observation is that the vapor depression threshold is lower than expected and is present across the entire range of typical LPBF energy densities; however, the formation of keyhole porosity is only present in cases where the vapor depression is deep and unstable [22,23].

There is a wide range of materials that have an optimized process parameter set (i.e., can be successfully printed) in commercial LPBF systems, including titanium (Ti) alloys [24], aluminum (Al) alloys [25–27], cobalt (Co) alloys [28], nickel (Ni) alloys [29,30], and stainless steels [31,32]. Among the stainless steels, duplex stainless steels (DSSs) are known for their excellent combination of corrosion resistance and mechanical properties in different environmental conditions and are widely used in petrochemical, marine, nuclear, and chemical applications [33]. DSSs microstructure has two phases, namely ferrite ( $\alpha$ ) and austenite ( $\gamma$ ) phases. Furthermore, it is important to maintain a roughly equal amount of ferrite and austenite phases (i.e., 1:1 ratio) to ensure high strength and enhanced corrosion resistance.

Recently, 2507 super duplex stainless steel (2507 SDSS) has gained considerable attention due to its high tensile and fatigue strength, good toughness, excellent pitting corrosion resistance, high weldability and formability, and high stress corrosion cracking resistance in chloride and sulfide environments, which is the reason for its wide adaptation in heat exchangers, desalination plants, and pressure vessels and boilers industry

systems [34]. In recent years, the adoption of LPBF in processing 2507 SDSS powder to manufacture highly dense parts with enhanced qualities has been investigated with success. Davidson et al. [35] studied the laser power influence on the resulting part quality and microstructure of 2507 SDSS. The scan speed, hatch distance, and layer thickness were kept constant at 590 mm/s, 120  $\mu\text{m}$ , and 50  $\mu\text{m}$ , respectively, while the laser power varied from 50 to 400 W resulting in an energy density range from 14.1 to 113  $\text{J}/\text{mm}^3$ . The resulting samples showed randomly distributed pores which were attributed to both insufficient melting at lower laser powers (i.e., lack of fusion pores) and entrapped gases at higher energy densities (i.e., keyhole pores). The highest reported sample density was 90.8% at an energy density of 70.62  $\text{J}/\text{mm}^3$  and the as-built sample microstructures were mainly ferritic with small amounts of austenite phases along the grain boundaries. Saeidi et al. [36] succeeded in manufacturing 2507 DSS samples with a relative density of 99.5% using a laser power of 190 W, scan speed of 750 mm/s, hatch distance of 100  $\mu\text{m}$ , and a layer thickness of 20  $\mu\text{m}$  with a reported energy density of 126.67  $\text{J}/\text{mm}^3$ . Kunz et al. [37] investigated the properties of 2507 SDSS manufactured by LPBF and reported a relative density of 99.6% using a laser power, scan speed, hatch distance, and layer thickness of 160 W, 1333.33 mm/s, 100  $\mu\text{m}$ , and 50  $\mu\text{m}$ , respectively with a calculated energy density of 24  $\text{J}/\text{mm}^3$ .

Considering the literature studies on 2507 SDSS, a full analysis of the laser power, scan speed, and hatch distance influence and their interactions during the manufacturing process on the resulting part quality and microstructure is not yet reported, which signifies clear research gaps. Furthermore, the current research studies on 2507 SDSS show a wide optimized energy density range from 24 to 126.67  $\text{J}/\text{mm}^3$  with fluctuating laser power, scan speed, and hatch distance parameter sets ranging from 160 to 250 W, 590 to 1333.33 mm/s, and 100 to 120  $\mu\text{m}$ , respectively [35–37]. As a result, it is challenging to decide which parameter set is the most reliable, and a need for a thorough 2507 SDSS parameter investigation is highlighted. In this study, the authors adopted the response surface method (RSM) to investigate the influence of laser power, scan speed, and hatch distance on the resulting sample quality and find an optimized parameter set capable of producing almost fully dense parts.

Statistical techniques, such as the RSM and analysis of variance (ANOVA), have been previously adopted and proven to be useful in the process parameter optimization of LPBF technology [38–40]. Wang et al. [38] investigated the LPBF process parameter effect on the sample microstructure and mechanical properties of a nickel-based superalloy using the RSM approach. They succeeded in increasing the resulting sample tensile strength by applying the RSM approach to optimize the process parameters. Ternier et al. [39] successfully optimized the laser power and scan speed process parameters to manufacture high-density CoCr-Mo alloy samples using RSM. Deng et al. [40] succeeded in manufacturing 316L samples with high density and low surface roughness by applying the RSM approach.

In summary, this paper investigates the influence of laser power, scan speed, and hatch distance on the resulting 2507 SDSS sample porosity (i.e., sample quality) fabricated by LPBF. High-resolution microcomputed X-ray tomography ( $\mu\text{CT}$ ) and optical microscope (OM) images were utilized to assess the resulting sample porosity and investigate the various pore formation types along the entire energy density range. The RSM approach is adopted to investigate the influence of each parameter and find a set of optimized printing parameters capable of manufacturing 2507 SDSS samples with minimum porosity (i.e., high density). Moreover, the microstructure and tensile properties of 2507 SDSS printed samples using the optimized process parameters are investigated as well. The findings of this study can be used as a stand-alone guide in selecting optimum printing process parameters to manufacture low porosity, high mechanical properties, and reliable 2507 SDSS samples using LPBF technique.

## 2. Materials and Methods

### 2.1. Material and Equipment

The SDSS 2507 powder produced by gas atomization is supplied by Sandvik Osprey (Neath, UK). The powder's chemical composition is shown in Table 1. The morphology of the powder particles significantly affects the fluidity and melting behavior of the powder in the LPBF process; parameters such as powder particle shape and size distribution influence the manufactured sample quality [1]. The Morphologi G3 shape image analyzer provided by Malvern Panalytical (Malvern, UK) is used in the characterization process of 2507 SDSS powder particles (Figure 1). Based on 113,626 counted particles, results showed that the particles are mostly spherical with a circularity mean of  $0.954 \pm 0.059$  (Figure 1b), where a circularity value of 1 depicts a complete spherical particle shape. The particle size distribution is shown in Figure 1c, with a mean particle diameter of  $28.63 \pm 9.04 \mu\text{m}$ .

**Table 1.** 2507 SDSS chemical composition.

Element	Fe	Cr	Ni	Mo	Mn	N	Si	Cu	C	P	S
Content (wt%)	Balance	24.6–25.4	6.8–7.2	3.76–4.24	0.7–1.1	0.26–0.31	0.2–0.6	0.20	0.02	0.025	0.008

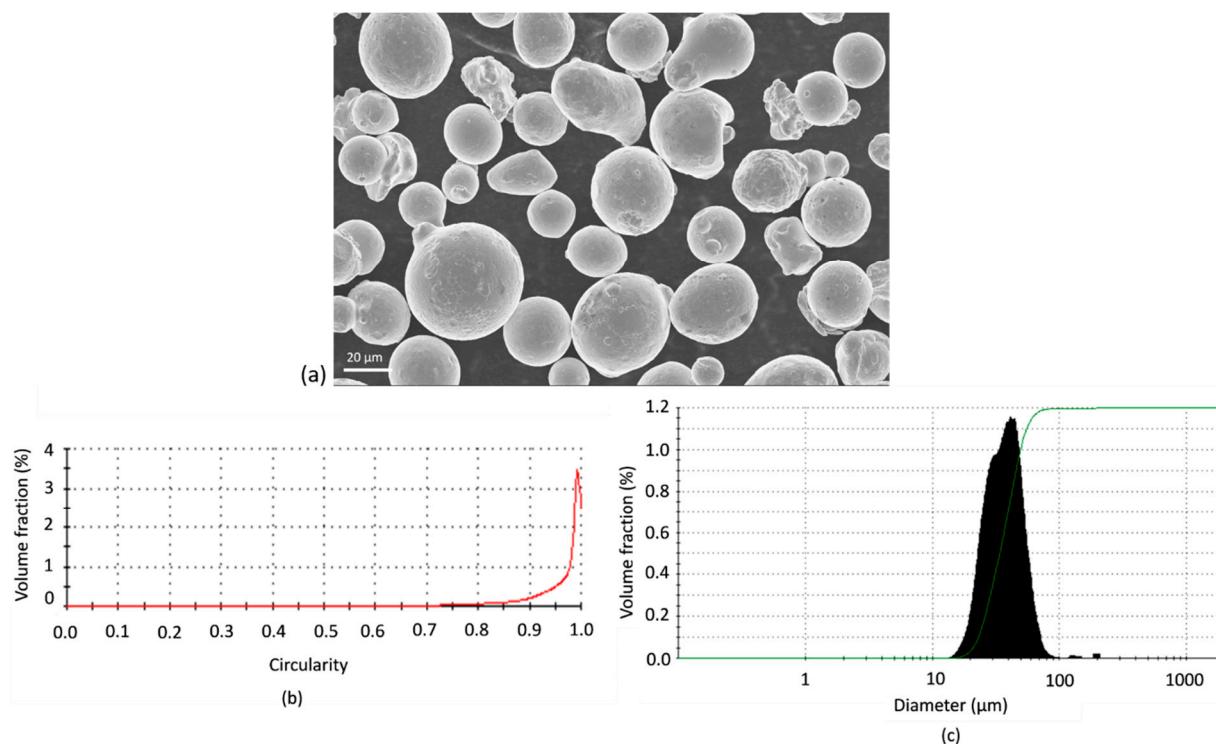


**Figure 1.** 2507 SDSS powder morphology: (a) microscopic image of 2507 SDSS powder particles; (b) powder particle circularity; (c) particle size distribution.

All samples were manufactured using the ORLAS Coherent 250W LPBF printer (Santa Clara, CA, USA). The ORLAS 250W printer uses an FLS 150 fiber laser with a wavelength of 1070 nm, a beam diameter of 40 μm, a laser power of up to 250 W, and a scanning speed of up to 3000 mm/s. The printing process of all samples was conducted in an argon environment with a constant oxygen level of 0.01%, and the scanning direction change between successive layers was kept at 45°.

### 2.2. Response Surface Methodology

RSM is a statistical approach that uses a design of experiment (DoE) for developing metrology, fitting a regression model between input and output parameters, and optimizing

the process outcomes [41]. The term “DoE” refers to a group of methods (full factorial, central composite, box-Behnken, etc.) for generating a set of trials whose outcomes are dependent on the input factors. In this study, three factors are optimized namely; laser power ( $p$ ), scan speed ( $v$ ), and hatch distance ( $h$ ), while the layer thickness ( $t$ ) is kept constant at 25  $\mu\text{m}$ . The layer thickness ( $t$ ) is usually overlooked in the optimization process and kept constant; However, enhanced qualities are observed with thin layer thicknesses [42], hence a layer thickness of 25  $\mu\text{m}$  was selected.

The selected DoE type determines the number of trials, combinations, replication, and randomization of the factors to investigate the cause-and-effect relationships between inputs and outputs with a certain level of confidence. Considering a full factorial DoE for three factors with five levels, the number of trials is  $5^3 = 125$ . However, manufacturing and measuring 125 trials (i.e., cubes) is not practical in terms of cost and time. The number of trials can be reduced to 20 using the central composite design (CCD) seen in Figure 2. The CCD is a sufficient five-level fractional factorial DoE with center and star points used to fit quadratic models. In a three-factor CCD, the model is composed of 8 factorial points (blue circles), a center point (red circle), and 6 star points which are at a distance ( $\alpha$ ) from the center point and are set to a default value of 1.6818 to ensure design rotatability as shown in Figure 2 (top view). The range of the factorial points (1, -1) for all three factors is identified based on the previous SDSS 2507 studies [36–38]. Then, the center and star points are calculated and reported, as seen in Table 2. The star points establish new low and high extreme values for all three factors. In this study, the center point was replicated six times to investigate the location effect on build plate on print quality. Minitab software (version 19, Minitab, Pennsylvania, USA) was utilized to generate the various run sets seen in Table 3 based on the CCD template shown in Figure 2. A total of 20 cubes with dimensions of (5 × 5 × 5) mm were designed, and each cube was assigned different printing parameters following the order seen in Table 3.

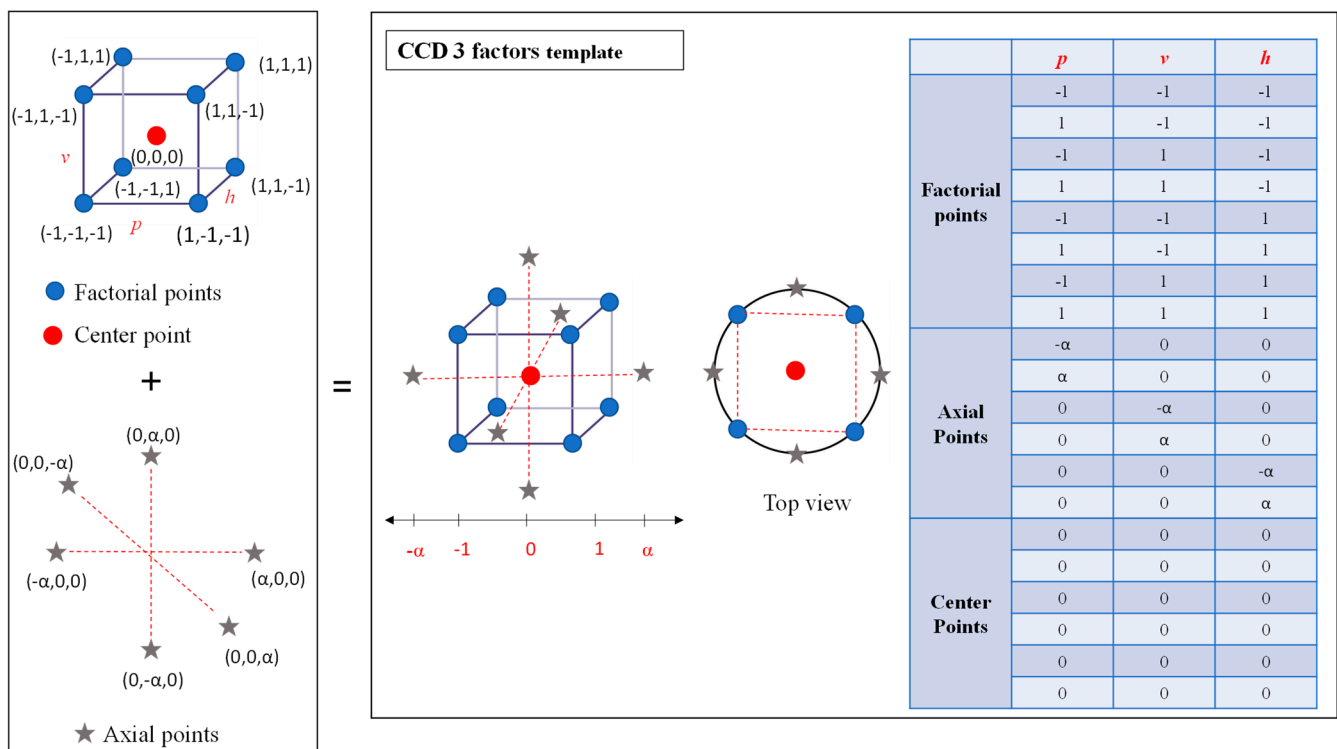


Figure 2. Schematic representation of a three-factor CCD.

**Table 2.** CCD factor levels and values.

Levels	Laser Power (W)	Scan Speed (mm/s)	Hatch Distance ( $\mu\text{m}$ )
Lowest ( $-\alpha$ )	69.3	159.1	26.1
Lower ( $-1$ )	100	500	50
Center point (0)	145	1000	85
Higher (1)	190	1500	120
Highest ( $\alpha$ )	220.7	1840.9	143.9
Range	69.3–220.7	159.1–1840.9	26.1–143.9

**Table 3.** CCD design set up for all factors.

Run	Laser Power (W)	Scan Speed (mm/s)	Hatch Distance ( $\mu\text{m}$ )
1	100	500	50
2	220.7	1000	85
3	145	1000	85
4	145	1000	85
5	190	1500	50
6	145	1000	85
7	145	1000	143.9
8	100	1500	50
9	69.3	1000	85
10	145	1000	85
11	190	500	120
12	190	1500	120
13	145	1000	85
14	190	500	50
15	145	1840.9	85
16	100	1500	120
17	100	500	120
18	145	1000	26.1
19	145	159.1	85
20	145	1000	85

Following the manufacturing process, the output (i.e., porosity) of all 20 manufactured samples is measured and analyzed; then, a polynomial quadratic regression model is fitted for each output using Minitab 19. The generalized quadratic regression model is defined as follows [41]:

$$Y = b_0 + \sum_{i=1}^n b_i x_i + \sum_{i=1}^n b_{ii} x_i^2 + \sum_{i < j} b_{ij} x_i x_j + e \quad (2)$$

where  $Y$  is the predicted response,  $x_i$  and  $x_j$  are the input factors;  $b_0$  is the intercept term,  $b_i$  is the linear term coefficient,  $b_{ii}$  is the squared term coefficient,  $b_{ij}$  is the interaction term coefficient, and  $e$  is the observed experimental error. The polynomial quadratic regression model is widely adopted as it considers non-linear effects and investigates the factor interaction influence on the predicted response. Following the acquisition of the polynomial regression model, adequacy and accuracy checking analysis is carried out to ensure that the fitted model is satisfying the regression assumptions and provides tolerable approximations of the response; then, analysis of variance (ANOVA) is utilized along with surface and contour plots to study the influence of input factors on the resulted porosity. Finally, the input factors are optimized using the regression model to produce minimum  $Y$  values (i.e., minimum porosity); a flow diagram summary of the RSM is seen in Figure 3.

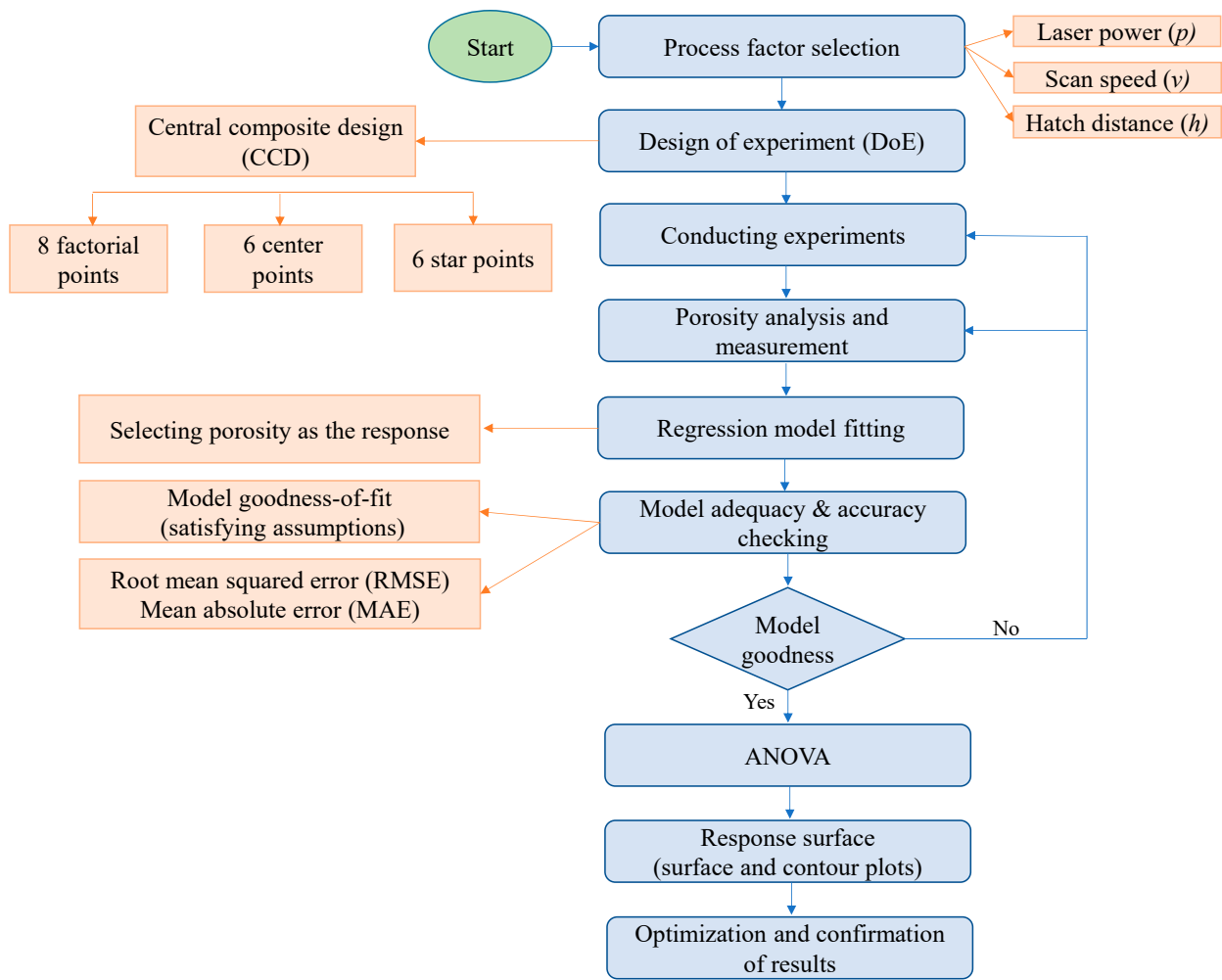


Figure 3. RSM flow diagram.

2.3. Mechanical Testing

Tensile strength analysis was conducted on manufactured tensile samples using the optimized parameter set that resulted from the RSM. A total of three cylindrical tensile samples were manufactured by the ORLAS Coherent 250W LPBF printer (Coherent, Santa Clara, CA, USA). The tensile specimens were designed according to the ASTM A370/ASME SA-370 standard with a total length of 80 mm and a testing diameter of 6.36 mm, as shown in Figure 4. The tensile testing was performed in a universal testing machine at room temperature (25 °C), with a strain rate of  $10^{-3} \text{ s}^{-1}$ .

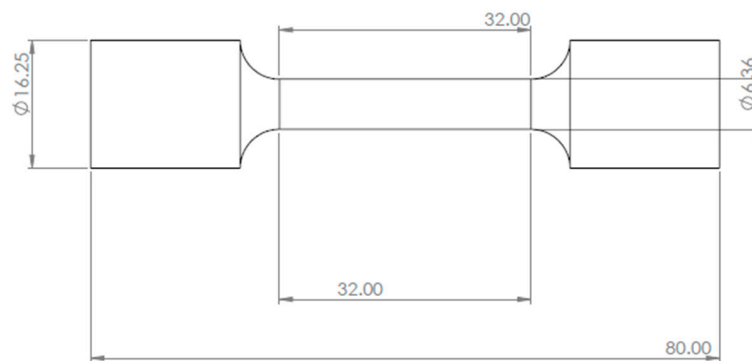
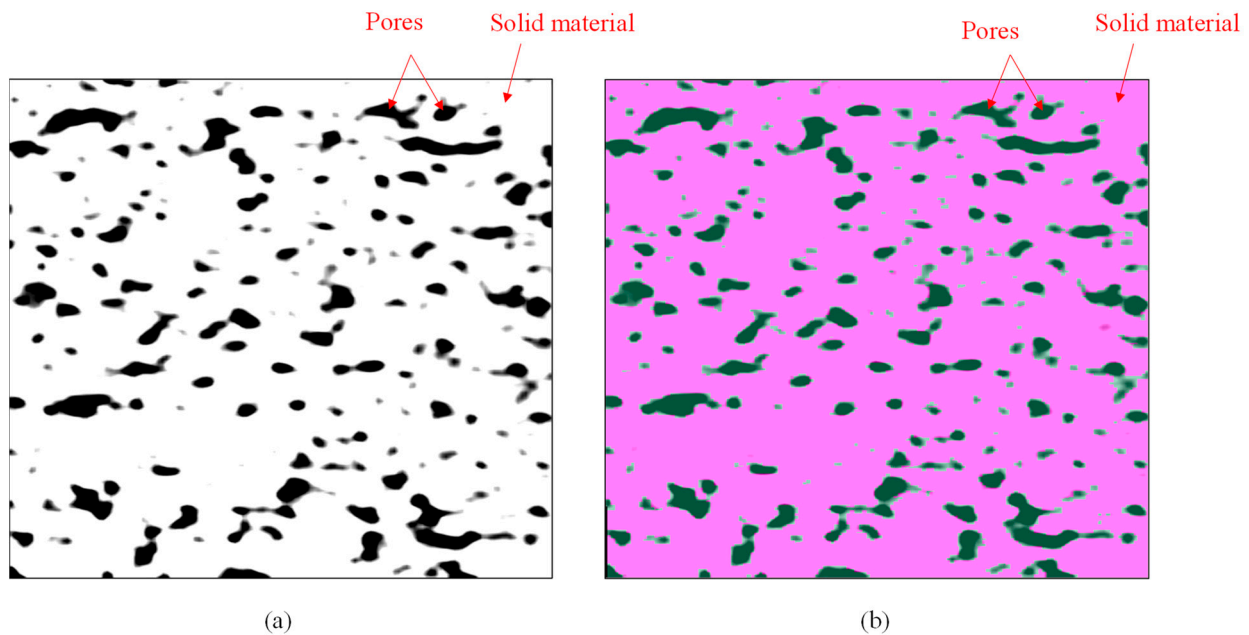


Figure 4. Tensile sample geometry dimensions (mm).

#### 2.4. Characterization Methods

High-resolution microcomputed X-ray tomography was utilized in the porosity characterization process. Using the ZEISS Xradia 620 Versa X-ray  $\mu$ CT (Oberkochen, Germany) with a voltage of 140 kV, a power of 21.01 W, and an exposure time of 3 s, micro CT reconstructed images were generated which revealed the inner porosity profile of the LPBF manufactured samples. Then, porosity characterization and quantification analysis were conducted using Dragonfly 21 software (version 21, Dragonfly, Montreal, Canada). Dragonfly porosity analysis is based on color-segmenting each layer of the 3D CT reconstructed images to distinguish between the solid material (purple) and pores (green), as shown in Figure 5. The Olympus optical microscope (Tokyo, Japan) was utilized to capture OM images for different pore types.



**Figure 5.** Dragonfly color segmentation process: (a) CT scanned image layer; (b) Color segmentation.

To observe the cross-section microstructure, samples were mounted and ground successively to 2000 grit, and then polished with diamond paste. After that, the polished specimens were etched in a 3 wt% Nital solution. Field Emission–Scanning Electron Microscope (FE-SEM), Zeiss Sigma (Gemie) was utilized for microstructural analysis. Furthermore, the XRD patterns were measured using a Rigaku Ultima IV diffractometer (Co K $\alpha$  radiation with a wavelength  $\lambda = 1.78886 \text{ \AA}$ ). Besides, a semi-quantitative analysis using reference intensity ratios (RIR) was performed for phase fraction which uses the ratio between intensity of the strongest peak of identified phase and the strongest peak of a standard (corundum was internationally used) in a 50-50 mixture (I/I<sub>c</sub>) to determine the abundance of that phase in a sample.

### 3. Results and Discussions

#### 3.1. Porosity Characterization Analysis

All 20 samples were successfully printed as seen in Figure 6. The resulting porosities for all samples were measured and reported in Table 4. Figures 7 and 8 show the various porosity formation regimes with increasing energy density. At lower energy densities, the melt pool and scan track become shallow and thin, causing a lack of fusion between adjacent tracks and successive layers, which results in the formation of large and irregular pores (i.e., lack-of-fusion pores) seen in Figure 8a–c. It can be observed that increasing the energy density resulted in a sharp decrease in the lack-of-fusion pores, where increasing the energy density from 22.22 J/mm<sup>3</sup> to 66.67 J/mm<sup>3</sup> showed a porosity reduction from

45.60% to 4.61% (Figure 7 “Red dots”). Following the lack-of-fusion regime, a narrow optimal energy density range from 68.24 J/mm<sup>3</sup> to 126.67 J/mm<sup>3</sup> (Figure 7 “green diamonds”) is observed in terms of porosity reduction with a porosity range from 0.33% to 0.04%. This intermediate regime is observed to have pores that are relatively small (Figure 8d,e), which are presumably attributed to trapped gas between powder particles (i.e., metallurgical pores). A gradual increase in the porosity is observed following the intermediate regime, with a porosity increase from 0.15% to 1.56% (Figure 7 “blue triangles”). The gradual increase in porosity is attributed to keyhole mode porosity seen in Figure 8f–h, which are present due to high energy densities that cause deep melt pools with strong dynamics resulting in entrapped pore vapors as the melt pool propagates.

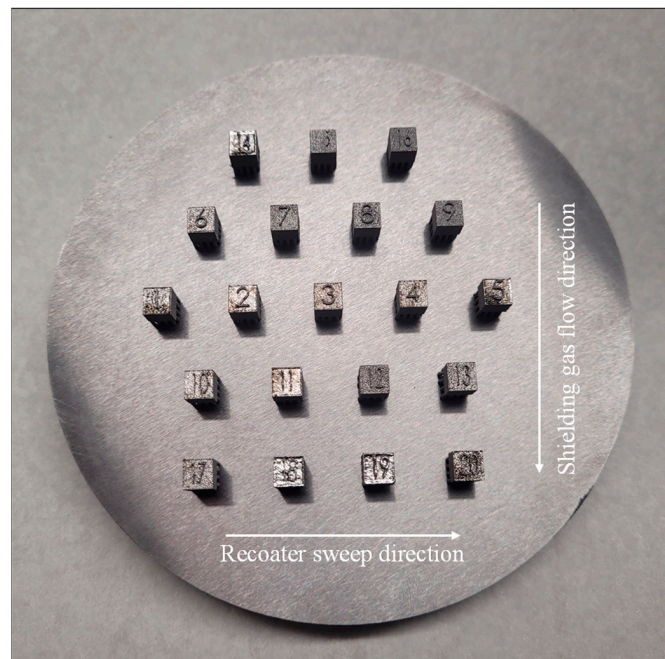


Figure 6. Successfully printed samples based on CCD and their positions on the substrate.

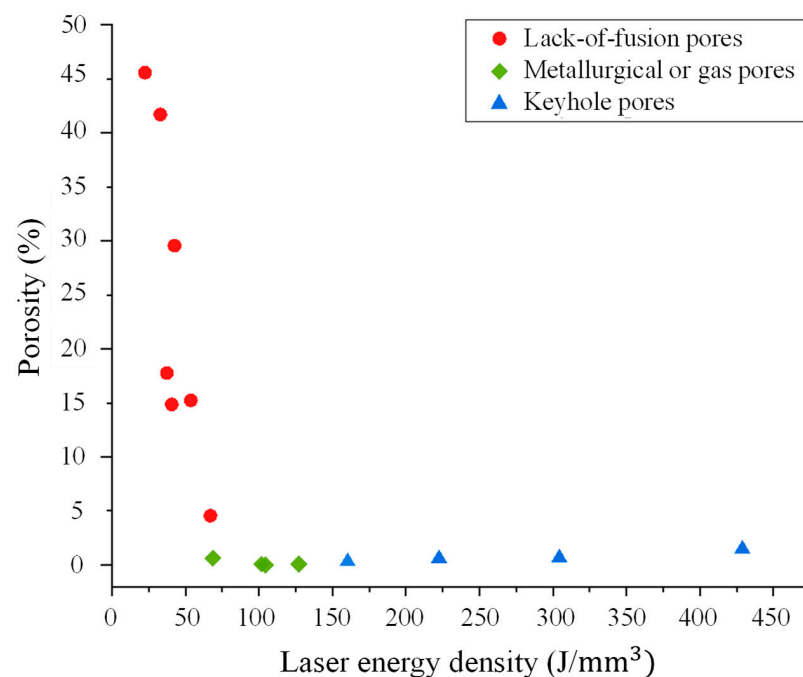
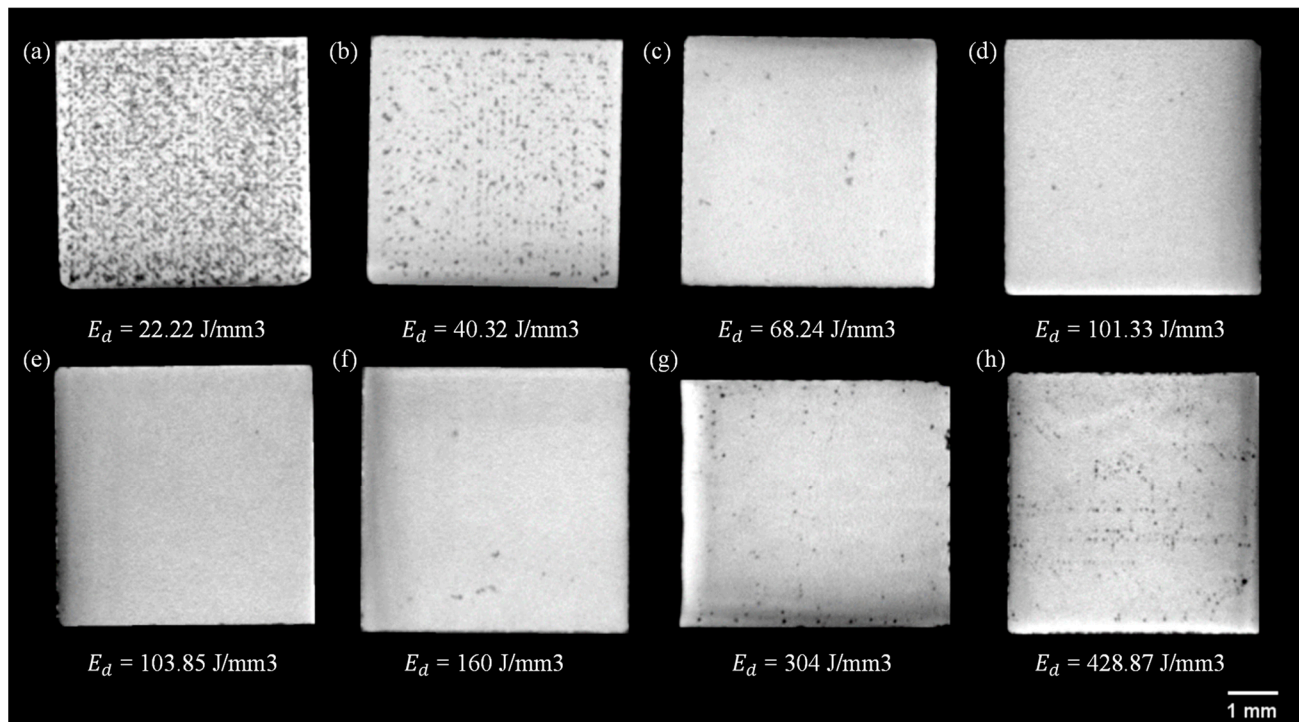


Figure 7. Porosity distribution with increasing energy density.



**Figure 8.** Cross-section CT images of sample series with increasing energy density.

**Table 4.** Porosity results.

Run	Laser Power (W)	Scan Speed (mm/s)	Hatch Distance ( $\mu\text{m}$ )	Layer Thickness ( $\mu\text{m}$ )	Laser Energy Density ( $\text{J}/\text{mm}^3$ )	Experimental Porosity (%)
1	100	500	50	25	160.00	0.36
2	220.7	1000	85	25	103.85	0.04
3	145	1000	85	25	68.24	0.69
4	145	1000	85	25	68.24	0.85
5	190	1500	50	25	101.33	0.13
6	145	1000	85	25	68.24	0.33
7	145	1000	143.9	25	40.32	14.92
8	100	1500	50	25	53.33	15.28
9	69.3	1000	85	25	32.62	41.74
10	145	1000	85	25	68.24	0.40
11	190	500	120	25	126.67	0.15
12	190	1500	120	25	42.22	29.60
13	145	1000	85	25	68.24	2.26
14	190	500	50	25	304.00	0.73
15	145	1840.9	85	25	37.07	17.80
16	100	1500	120	25	22.22	45.60
17	100	500	120	25	66.67	4.61
18	145	1000	26.1	25	221.91	0.66
19	145	159.1	85	25	428.87	1.56
20	145	1000	85	25	68.24	3.01

Examining the replicated center point samples (i.e., samples 3, 4, 6, 10, 13, and 20 based on Table 3) having a constant laser energy density of  $68.24 \text{ J}/\text{mm}^3$ , it is evident from porosity readings that the sample location influences the resulting porosity. Although samples 3, 4, 6, and 10 showed relatively close porosity readings within the 0.33% to 0.85% range. However, samples 13 and 20 are observed to experience significant irregularity in porosity readings with 2.26% and 3.01%, respectively. This can be attributed to positioning these samples farthest from the shielding gas and recoater sweep directions as seen in Figure 6, resulting in insufficient shielding gas and powder spread which can adversely affect the

resulting sample density. Davidson and Ferrar et al. [35,43] reported similar observations and attributed the behavior to the sample location from the sweep and shielding gas directions. One distinct note they reported is that the argon flow rate is higher at the plate's front and decreases along the back, which leads to insufficient condensate vapor removal causing incident laser radiation absorption or laser beam scattering that results in surface semi-sintered particles. As such, it is always favorable to position the samples in the middle of the build plate whenever possible.

Further quantitative porosity analysis is conducted for the lack-of-fusion, metallurgical or gas, and keyhole pore regimes based on samples 16, 2, and 19 with energy densities of 22.22 J/mm<sup>3</sup>, 103.85 J/mm<sup>3</sup>, and 428.87 J/mm<sup>3</sup>, respectively. The pore size and shape for each regime are summarized in Table 5 in terms of feret diameter and aspect ratio, respectively. The aspect ratio is a value between 0 to 1 and provides insights into the pore shape where a low aspect ratio (less than 0.5) indicates a flat-like shape (i.e., irregular), and a high aspect ratio (higher than 0.5) is an indication of spherical pores. The lack-of-fusion pores are observed to be relatively large and have irregular shapes with a mean feret diameter and mean aspect ratio of 0.26 mm and 0.33, respectively. This is clearly seen in Figure 9a,d, with large irregular-shaped pores having trapped unmelted powder particles, hence the resulting high porosity of 45.6%. As the energy density increases from 22.22 to 103.85 J/mm<sup>3</sup>, an optimal intermediate regime is observed having relatively small and spherical pores shown in Figure 9b,e with a mean feret diameter and mean aspect ratio of 0.05 mm and 0.65, respectively. Following the intermediate regime and as the energy density increases from 103.85 J/mm<sup>3</sup> to 428.84 J/mm<sup>3</sup>, a gradual increase in pores is observed which is attributed to keyhole pores at higher energy densities. The pores are observed to be roundish and slightly larger than the metallurgical or gas pores (i.e., intermediate regime) shown in Figure 9c,f with a mean feret diameter and aspect ratio of 0.09 mm and 0.57, respectively.

**Table 5.** Pore shape and size in terms of aspect ratio and feret diameter.

Sample	16			2			19		
Power (w)	100			220.7			145		
Scan speed (mm/s)	1500			1000			159.1		
Hatch distance (μm)	120			85			85		
Layer thickness (μm)				25					
Laser energy density (J/mm <sup>3</sup> )	22.22			103.85			428.87		
Pore type	Lack of fusion			Metallurgical or gas			Keyhole		
Feret diameter (mm)	Min.	Max.	Mean	Min.	Max.	Mean	Min.	Max.	Mean
	0.12	0.77	0.26 ± 0.12	0.04	0.06	0.05 ± 0.01	0.04	0.13	0.09 ± 0.02
Aspect ratio	Min.	Max.	Mean	Min.	Max.	Mean	Min.	Max.	Mean
	0.05	0.76	0.33 ± 0.14	0.59	1	0.65 ± 0.08	0.20	0.81	0.57 ± 0.17
Porosity %	45.60			0.06			1.56		

### 3.2. Response Surface Methodology Analysis

#### 3.2.1. Regression Model Equation

A quadratic regression model is developed which correlates the laser power ( $p$ ), scan speed ( $v$ ), and hatch distance ( $h$ ) with the response (i.e., porosity) based on Equation (2). Using Minitab 19 software, the input factors ( $p$ ,  $v$ ,  $h$ ) and experimental porosity results seen in Table 4 were used as the base for the fitted regression model. The multiple regression analysis techniques found in RSM are used to estimate the model's coefficients, and the response can be expressed by the following quadratic Equation:

$$\text{Porosity (\%)} = 88.5 - 0.901(p) - 0.0155(v) - 0.399(h) + 0.003166(p^2) + 0.00001(v^2) + 0.00145(h^2) - 0.00015(p.v) - 0.00046(p.h) + 0.000401(v.h) \quad (3)$$

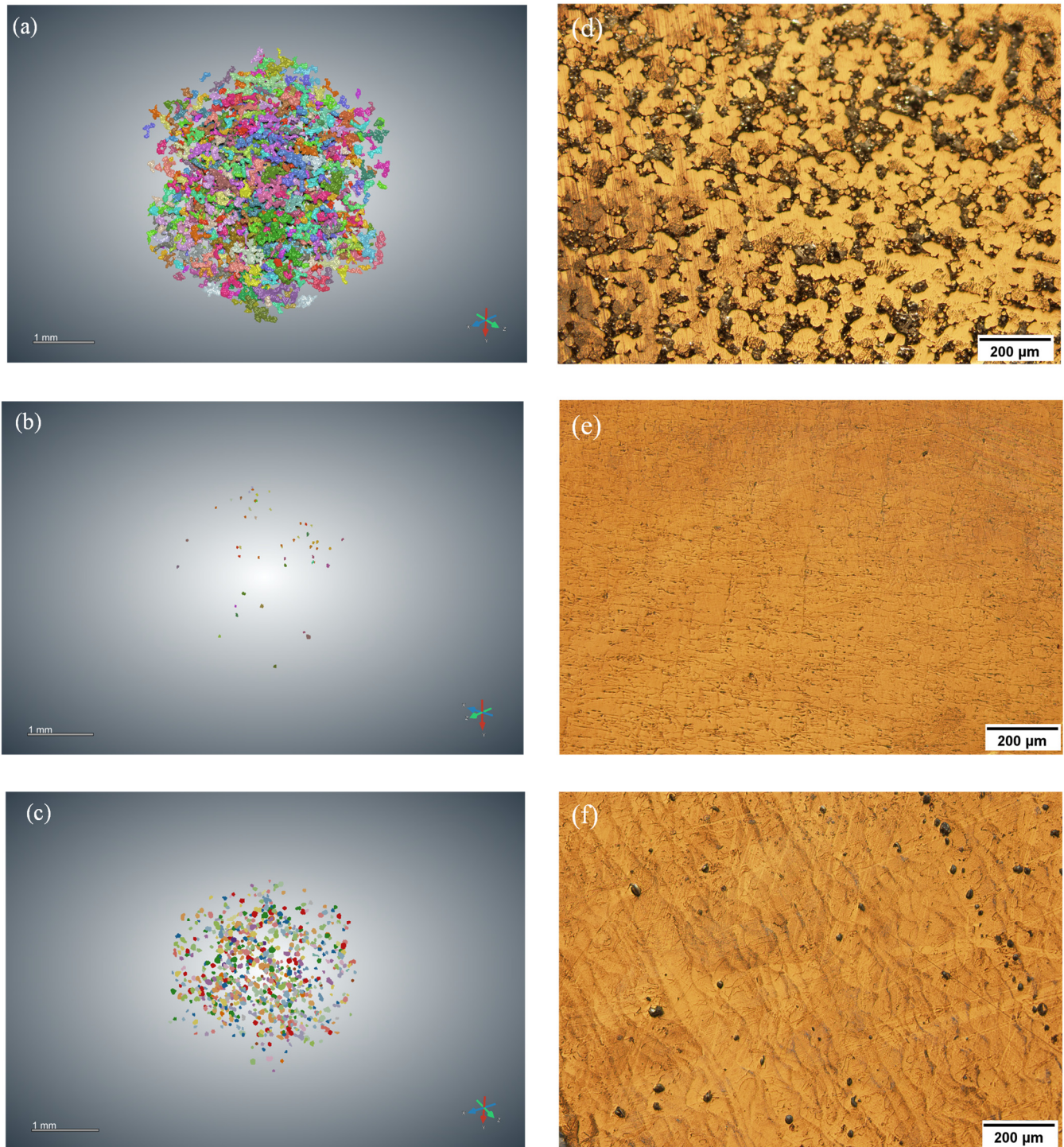


**Figure 9.** Lack-of-fusion (sample 16), metallurgical or gas (sample 2), and keyhole (sample 19) pores: (a–c) 3D representation; (d–f) OM images.

### 3.2.2. Model Adequacy and Accuracy Checking

Model adequacy and accuracy checking is essential to check the fitted model and ensure that it provides a fair approximation of the porosity response. Unless the regression model shows an adequate fit, the analysis or optimization of the fitted response may result

in poor or inaccurate outcomes. The model adequacy is checked using the residuals, which result from the difference between the observed values and fitted values predicted by the regression model. The normal probability plot of the residuals seen in Figure 10a is one way to check if the model satisfies the normality assumption. It can be observed that the normality assumption is valid and satisfied as the residuals are approximately distributed along a straight line. Figure 10b shows the predicted values distribution versus the residuals. It is evident that the residuals are randomly distributed with no obvious trends, suggesting a constant variance between the residuals. Therefore, the model satisfies the constant variance assumption.

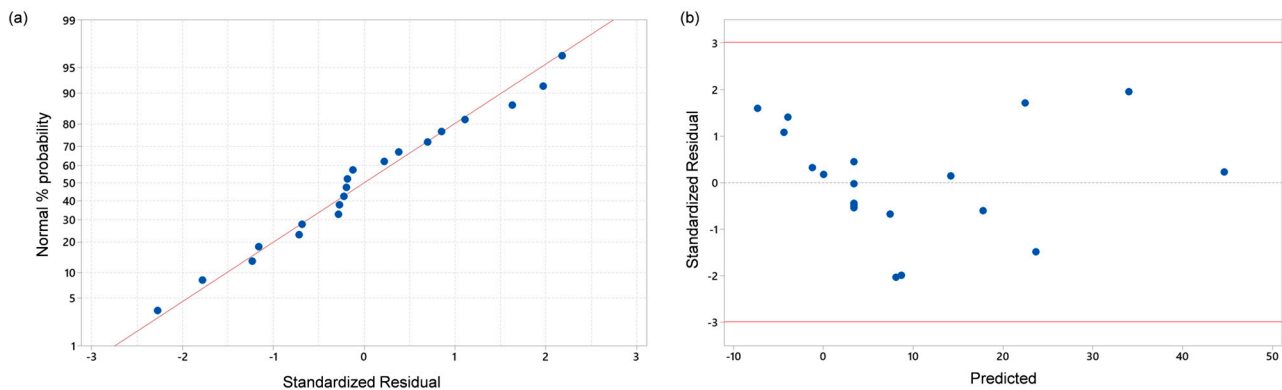


**Figure 10.** (a) Normal probability plot of the residuals; (b) Predicted values vs. residuals.

The regression model accuracy is evaluated using metrics such as the root mean squared error (RMSE) and mean absolute error (MAE), which are calculated according to Equations (4) and (5):

$$\text{RSME} = \left( \frac{1}{n} \sum_{i=1}^n (Y_{i\text{actual}} - Y_{i\text{predicted}})^2 \right)^{0.5} \quad (4)$$

$$\text{MAE} = \frac{1}{n} \sum_{i=1}^n |(Y_{i\text{actual}} - Y_{i\text{predicted}})| \quad (5)$$

where  $n$  is the number of samples,  $Y_{i\text{actual}}$  is the resulting experimental porosity, and  $Y_{i\text{predicted}}$  is the predicted porosity using the regression model. The RSME and MAE results for the developed regression model are within the acceptable range with values of 4.735% and 3.917%, respectively. The model adequacy and accuracy results are satisfactory; therefore, it can be concluded that the regression model's fitting is sufficient to describe the porosity response.

### 3.2.3. ANOVA and Response Surface Analysis

The ANOVA analysis results seen in Table 6 indicate the statistical data of the regression model. The significance of each calculated regression coefficient is tested and evaluated. These tests indicate whether the terms significantly influence the response values. The  $p$ -value test results seen in Figure 11 show how significant the effect of each term is on the resulting porosity, where a calculated  $p$ -value of less than 0.05 is an indication that the term has a statistical significance of 95% confidence level. It is evident that the linear terms of laser power, scan speed, and hatch distance have a significant effect on the resulting porosity with  $p$ -values of 0.001, 0.001, and 0.004, respectively. The non-linear effect (i.e., squared term) is only observed to be significant for the laser power with a  $p$ -value of 0.003, whereas higher  $p$ -values of 0.173 and 0.311 are seen for the scan speed and hatch distance, respectively, indicating that the non-linear effect of these factors is not significant. This can be observed from the factor vs. porosity main effect plots seen in Figure 12a, where a stronger parabolic trend is seen with the laser power than with speed and hatch factors. Furthermore, the power vs. porosity plot additionally shows the sharp porosity decrease

when increasing the power from 69.3 W to around 150 W, followed by a gradual increase in porosity for higher power values. Anton [23] reported a similar observation with increasing the laser power, where he stated a very sharp lack of fusion porosity drop at low laser power values followed by a gradual increase in keyhole porosity at higher power values. Moreover, the speed vs. porosity and hatch vs. porosity plots (Figure 12a) indicate that increasing the scan speed and hatch distance results in higher porosity profiles.

Table 6. Model ANOVA results.

Source	DF	Adj SS	ADJ MS	F-Value	p-Value
Model	9	3438.74	382.082	9.53	0.001
Linear	3	2294.29	764.762	19.07	0.000
A-Power (W)	1	814.20	814.198	20.30	0.001
B-Speed (mm/s)	1	920.97	920.971	22.97	0.001
C-Hatch (µm)	1	559.12	559.118	13.94	0.004
Square	3	654.37	218.123	5.44	0.018
AA	1	592.51	592.508	14.78	0.003
BB	1	86.42	86.424	2.16	0.173
CC	1	45.62	45.622	1.14	0.311
2-Way interaction	3	490.08	163.360	4.07	0.039
AB	1	91.09	91.091	2.27	0.163
AC	1	4.14	4.143	0.10	0.755
BC	1	394.85	394.847	9.85	0.011
Error	10	401.02	40.102		
Lack-of-fit	5	375.03	75.006		
Pure Error	5	25.99	5.198		
Total	19	3839.76			

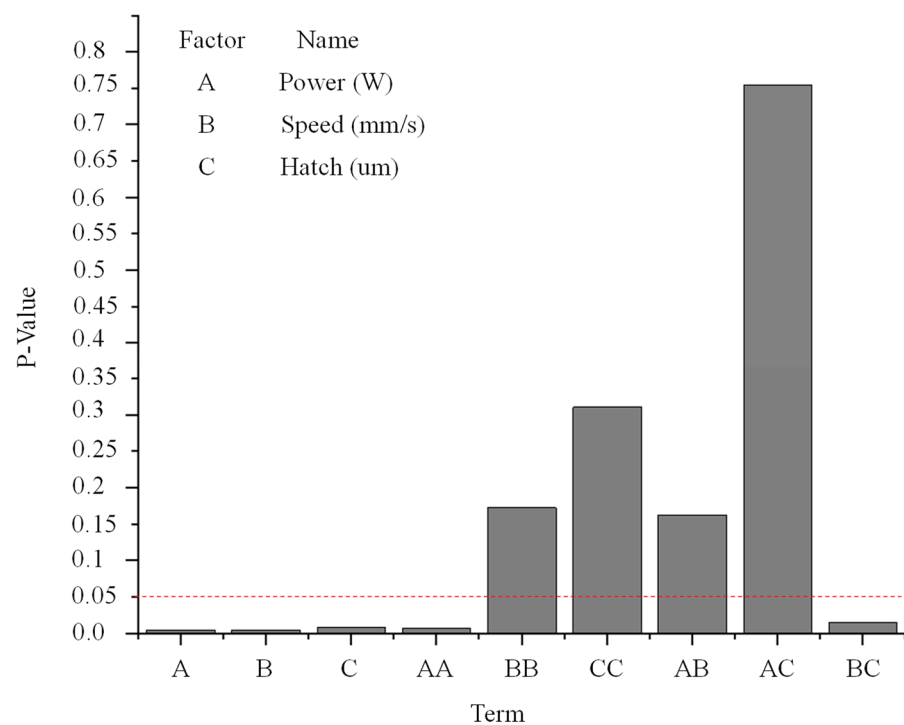


Figure 11. p-values of regression model terms.

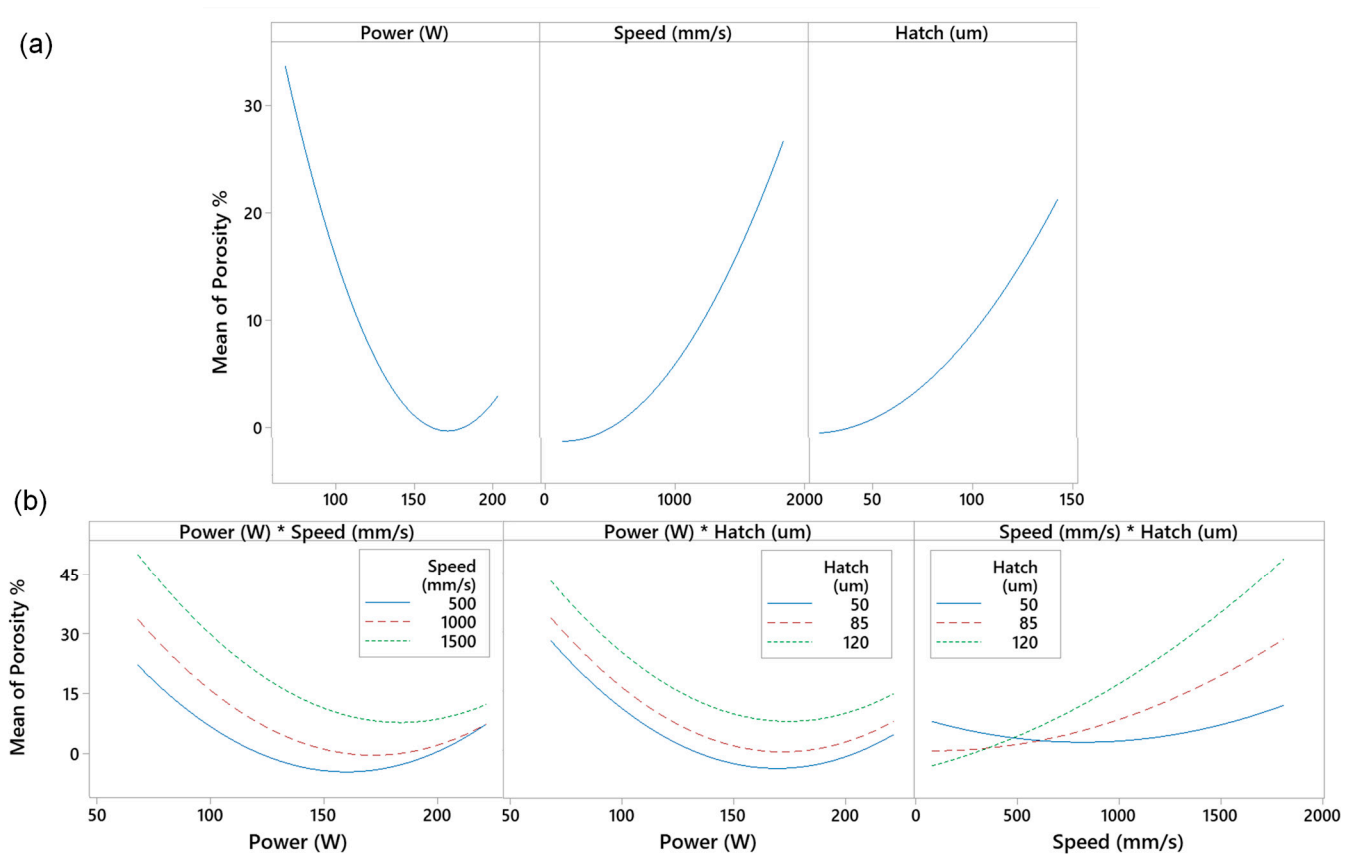
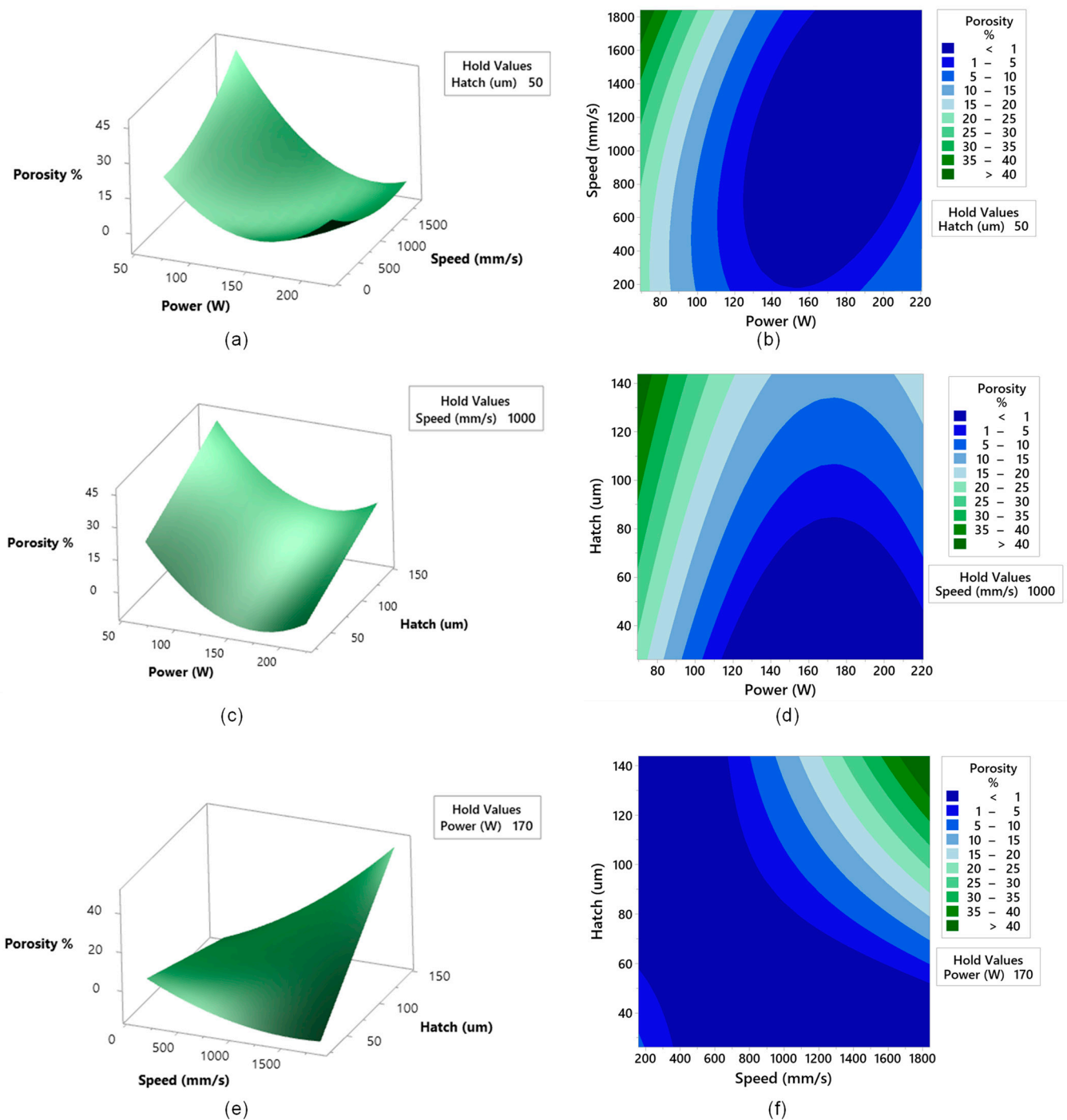


Figure 12. Factor vs. porosity plots: (a) Main effects; (b) Interaction.

Regarding the interaction term and as shown in Figure 11, the factor interaction between speed and hatch (BC) is observed to be significant with a  $p$ -value of 0.011, whereas interactions between power and speed (AB), and power and hatch (AC) are observed to be insignificant with  $p$ -values of 0.163 and 0.755, respectively. This can be observed from the factor vs. porosity interaction plots shown in Figure 12b, where increasing the laser power seems to not influence the speed and hatch curves seen in the (power\*speed) and (power\*hatch) plots. However, as seen from the (speed\*hatch) plot, increasing the speed is observed to influence the various hatch curves, which indicates a strong interaction effect between the speed and hatch factors.

Based on the regression model, three-dimensional (3D) surface graphs and equivalent contour plots seen in Figure 13 were generated to illustrate the influence of each process parameter (i.e., factors) on the resulting sample porosity. The influence of laser power and scan speed on the porosity is shown in Figure 13a,b at a fixed hatch distance of 50  $\mu\text{m}$ . It can be observed that higher porosities are seen with decreasing the laser power and increasing the scan speed. When the laser power goes to less than 80 W and the scan speed higher than 1400 mm/s, the porosity is observed to be higher than 35%. This can be attributed to the resulting low energy density with, respectively, lower and higher laser power and scan speed values leading to lack-of-fusion pores. Although increasing the laser power while decreasing the scan speed shows a reducing trend in the porosity; however, having extreme higher laser power and lower scan speed settings is observed to adversely influence the sample density with a porosity range from 1 to 10%. This can be attributed to the resulting higher energy densities and the associated keyhole pores. This indicates that extreme low laser powers coupled with high scan speeds or extreme high laser powers coupled with low scan speeds should be avoided during the LPBF process to reduce the resulting print porosity (i.e., improve the sample density).



**Figure 13.** Laser power, scan speed, and hatch distance influence on the porosity: (a,c,e) surface plots; (b,d,f) counter plots.

Figure 13c,d show the effect of laser power and hatch distance on the porosity at a fixed scan speed of 1000 mm/s. It is evident that a combination of low laser power and high hatch distance results in a significant increase in the resulting porosity. This can be observed when setting the laser power to less than 80 W and the hatch distance higher than 120  $\mu\text{m}$ , which resulted in a porosity profile higher than 40%. This is attributed to having significantly low energy densities (less than  $22.86 \text{ J/mm}^3$ ) leading to the prominent presence of lack-of-fusion pores, which indicates that lower laser power and higher hatch distance settings should be avoided. Generally, high hatch distances must be avoided as it can cause insufficient laser overlap leading to poor melting of the powder. This can

be observed at the higher ends of the laser power and hatch distance porosity profiles in Figure 13c,d. Although the energy density is sufficient ( $E_D = 73.33 \text{ J/mm}^3$ ) having a laser power and hatch distance of 220 W and 120  $\mu\text{m}$ , respectively. However, a high porosity profile (10–15%) is observed, which can be attributed to the formation of lack-of-fusion pores due to the poor melting resulting from insufficient laser overlap at high hatch distances.

Figure 13e,f show the effect of the scan speed and hatch distance on the resulting porosity at a fixed laser power of 170 W. It can be observed that higher scan speeds coupled with high hatch distances result in high porosity profiles. This is seen when setting the scan speed and hatch distance to 1800 mm/s and 140  $\mu\text{m}$ , respectively, which resulted in a porosity profile higher than 40%. Although decreasing the scan speed and hatch distance results in a reduction in the porosity. However, setting extremely low scan speeds and hatching distances is observed to increase the porosity, which is attributed to the resulting high energy densities causing instabilities in the melt pool and the formation of keyhole pores. This indicates that extreme high scan speeds coupled with high hatch distances or extreme low scan speeds coupled with low hatch distances should be avoided to maintain low porosity profiles during the LPBF printing process.

### 3.2.4. Parameter Optimization for Porosity

The laser power, scan speed, and hatch distance parameters were optimized to achieve minimum porosity outcomes. In order to increase the model's prediction accuracy, the highest non-significant terms (AC and CC) were eliminated from the regression model, as seen in Equation (6):

$$\text{Porosity (\%)} = 82.5 - 0.915(p) - 0.0141(v) - 0.219(h) + 0.003079(p^2) + 0.000009(v^2) - 0.00015(p.h) + 0.000401(v.h) \quad (6)$$

Minitab 19 was utilized to generate three optimized parameter sets capable of producing samples with minimum porosities at an identified porosity range from 0% to 1%, as seen in Table 7. All three optimized sets (1, 2, and 3) have a fixed layer thickness of 25  $\mu\text{m}$  with a calculated energy density of 142.72  $\text{J/mm}^3$ , 97.69  $\text{J/mm}^3$ , and 87.16  $\text{J/mm}^3$ , respectively. Three replicated samples were manufactured for each set at different locations (Figure 14) to validate each optimized parameter set. The samples were organized into columns (left, middle, and right) where each column has different position patterns (closest, middle, and farthest) from the shielding gas direction, as seen in Figure 14.

**Table 7.** Optimized parameter sets for minimal porosity.

Set/Sample	Power (W)	Speed (mm/s)	Hatch ( $\mu\text{m}$ )	Predicted Porosity (%)
1	209.6	1022.9	57.4	0.141
2	217.4	1735.7	51.3	0.039
3	145	1000.0	87.16	0.047

Table 8 shows the experimental porosity results based on the optimized combination of printing parameters. It can be observed that the three sets produced almost fully dense samples with relative densities higher than 99.837% (i.e., porosities less than 0.163%). Furthermore, the experimental porosity results agree well with the predicted values, with a maximum reported residual of 0.032, indicating the possibility of successfully predicting the porosity using the regression model. One distinct observation is that the first sample row closest to the shielding gas showed superior porosity results compared to the other replicates (Table 8, green highlighted), which indicates that the shielding gas direction effect is more significant than the sweep direction. Figure 15 shows cross-section CT images of the optimized first row samples. Sample 1 showed higher porosity results than samples 2 and 3, which can be attributed to the relatively higher energy density of 142.72  $\text{J/mm}^3$  that resulted in the formation of keyhole pores seen in Figure 14a. Sample 2 (Figures 15b and 16) with a laser power, scan speed, and hatch distance of 217.4 W, 1735.7 mm/s, and 51.3  $\mu\text{m}$ , respec-

tively, showed optimal reduced porosity results of 0.011% (i.e., a relative density of 99.989%). As a result, set 2 was selected as the optimized printing parameters for 2507 SDSS and was adopted in printing the tensile samples for tensile strength property characterization.

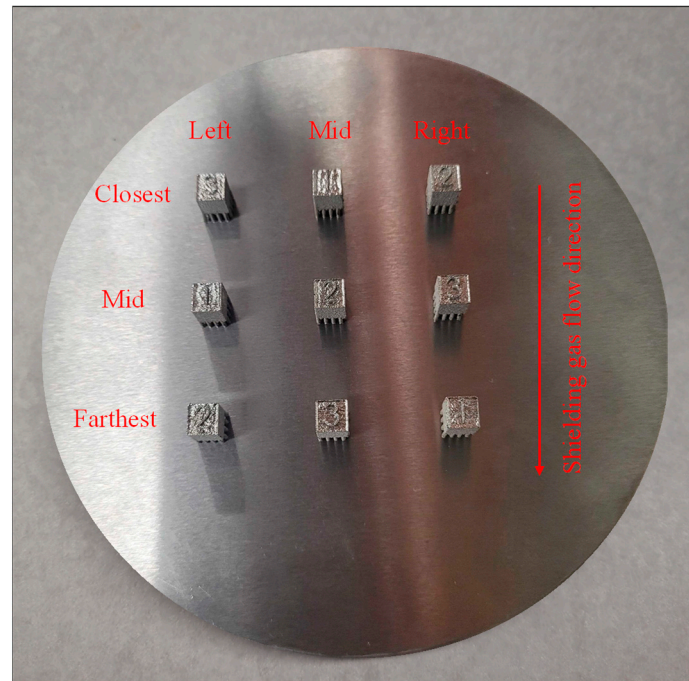


Figure 14. Manufactured optimized samples.

Table 8. Optimized parameters experimental vs. predicted porosity results.

Set/Sample	Power (W)	Speed (mm/s)	Hatch ( $\mu\text{m}$ )	Experimental Porosity			Avg.	Predicted Porosity	Residual
				Left	Mid	Right			
1	209.6	1022.9	57.4	0.167	0.055	0.266	0.163	0.141	0.022
2	217.4	1735.7	51.3	0.029	0.030	0.011	0.023	0.039	-0.016
3	145	1000.0	87.16	0.040	0.139	0.058	0.079	0.047	0.032

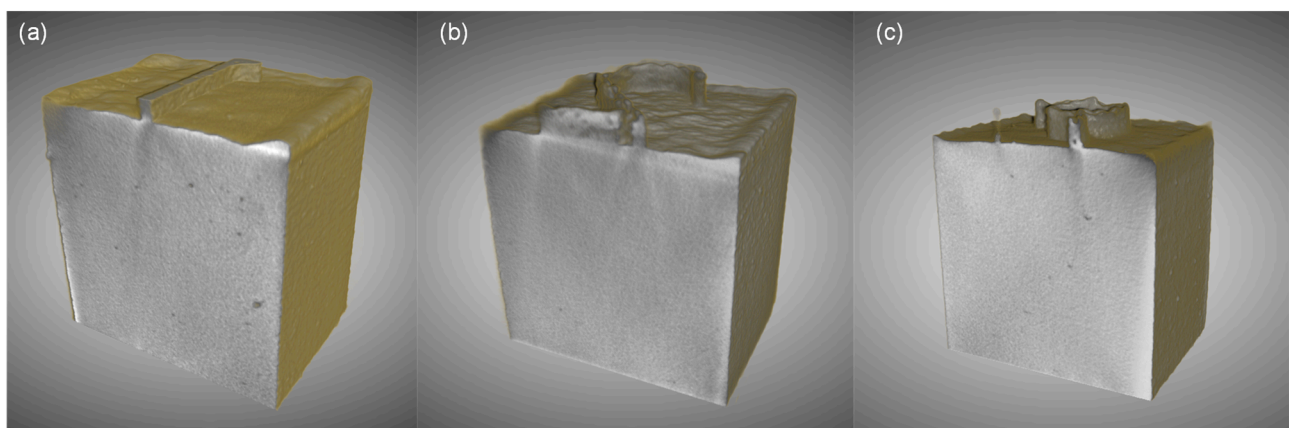
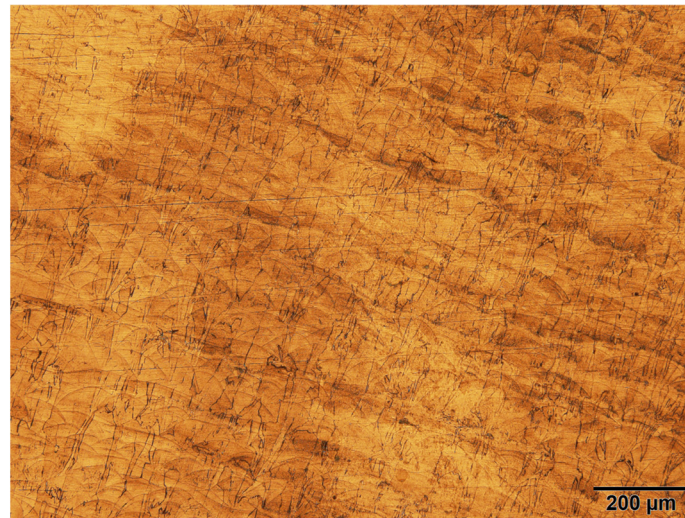


Figure 15. Cross-section CT images of optimized first row samples: (a) Sample 1; (b) Sample 2; (c) Sample (3).



**Figure 16.** OM image of Set 2 optimized parameters.

### 3.3. Microstructure Analysis

The XRD patterns of 2507 SDSS in different process parameters employed in the LPBF process are depicted in Figure 17. Duplex stainless steels consist of ferrite (bcc) and austenite (fcc) phases. The formation of the ferritic microstructure is followed by nucleation of the austenite phase at grain boundaries of the ferrite grains during the cooling cycle [33]. However, due to insufficient time as a result of the high cooling rate in the LPBF process, the phase transformation from ferrite to austenite is not favorable and this rapid cooling cycle in the LPBF process cause excessive ferritization. As can be seen, with the increase of energy density during the LPBF process, the diffraction intensities of the ferrite phase increase. Ferrite phase fraction increased from 73 % to 89.3 % and then 94.7 % with the increase of energy density from 22.22 J/mm<sup>3</sup> to 97.69 J/mm<sup>3</sup> (optimized set) and then 428.87 J/mm<sup>3</sup>, respectively. The reason for this change of ferrite fraction with the increase of energy density could be related to chemical composition change due to extremely high melt pool temperatures. It can be assumed that with increase of energy density, austenite stabilizer elements such as N during LPBF processing will be vaporized and reduce the austenite content [44]. However, in order to get an optimal phase balance and restore the equilibrium duplex microstructure and mechanical properties of DSSs, post-processing heat treatment is recommended.

Kunz et al. [37] investigated the microstructure of LPBF produced 2507 SDSS parts and they found out that ferrite is the dominant phase and there is a limited amount of austenite in grain boundaries after the LPBF process. In order to increase the austenite fraction in duplex stainless steel, further solution annealing and heat treatment are recommended as Kunz et al. achieved 43.3% austenite fraction after solution annealing. In another study on 2205 SDSS with chemical composition close to 2507, Haghdadi et al. [45], reported austenite fraction of 2% mostly distributed in grain boundaries after LPBF process. Furthermore, they observed austenite promotion of 45% after heat treatment.

Figure 18 shows the microstructure evolution of the 2507 SDSS specimens at optimum energy density along the building direction. As Kunz et al. [37] observed in their study, the square-like microstructure can be seen along the building direction which is due to the scanning strategy during the LPBF process. In another study, Nigon et al. [46] observed the same kind of square-like microstructure along the building direction of 2205 SDSS parts produced by LPBF.

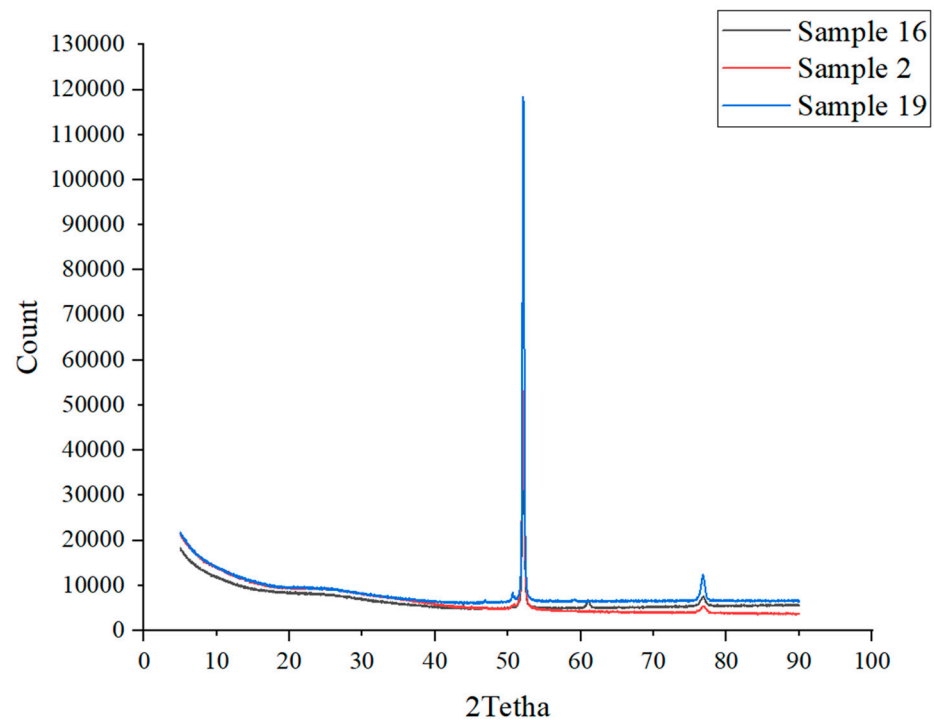
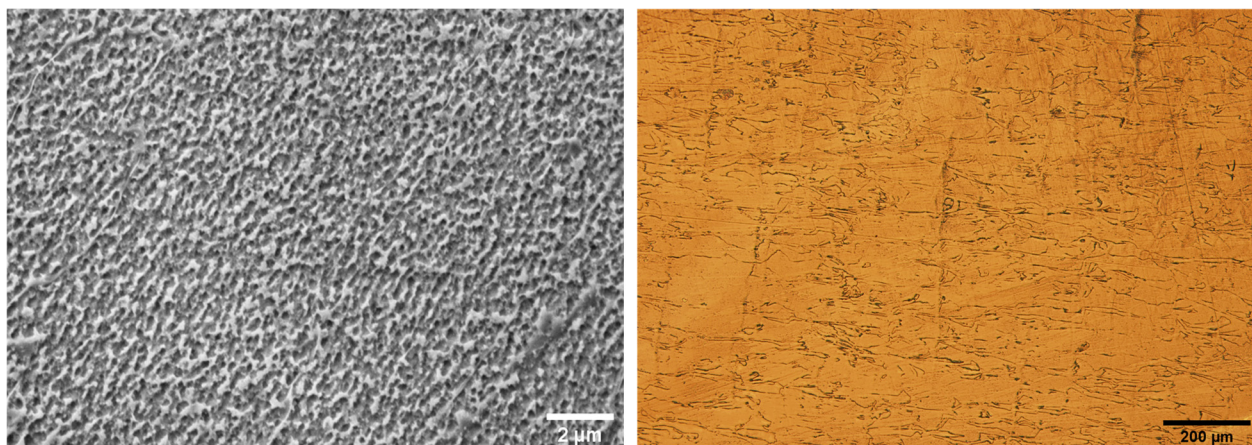


**Figure 17.** XRD patterns of 16, 2 (optimized), and 19 2507 SDSS samples.



(a)

(b)

**Figure 18.** Microstructure evolution of the 2507 SDSS specimens at optimum energy density; (a) SEM image, (b) OM image.

### 3.4. Tensile Strength Analysis

The printed tensile samples using the optimized printing parameters are shown in Figure 19, and the resulting yield strength, ultimate tensile strength (UTS), and elongation tensile properties are reported in Table 9. Figure 20 presents the tensile stress-strain curves of the printed tensile samples. Sample 1 exhibited the highest yield and ultimate tensile strength of 1254.50 MPa and 1403.10 MPa, respectively, followed by sample 2 with a yield and ultimate tensile strength of 1131.70 MPa and 1366.70 MPa, respectively. However, sample 3 exhibited the lowest tensile properties with a yield and ultimate strength of 960.10 MPa and 1000.30 MPa, respectively. This behavior can be attributed, as mentioned before, to the position of each sample from the shielding gas. As shown in Figure 19, sample 3 is positioned farthest from the shielding gas, leading to an insufficient shielding gas flow rate which adversely affects the sample density (i.e., causing reduced mechanical results).

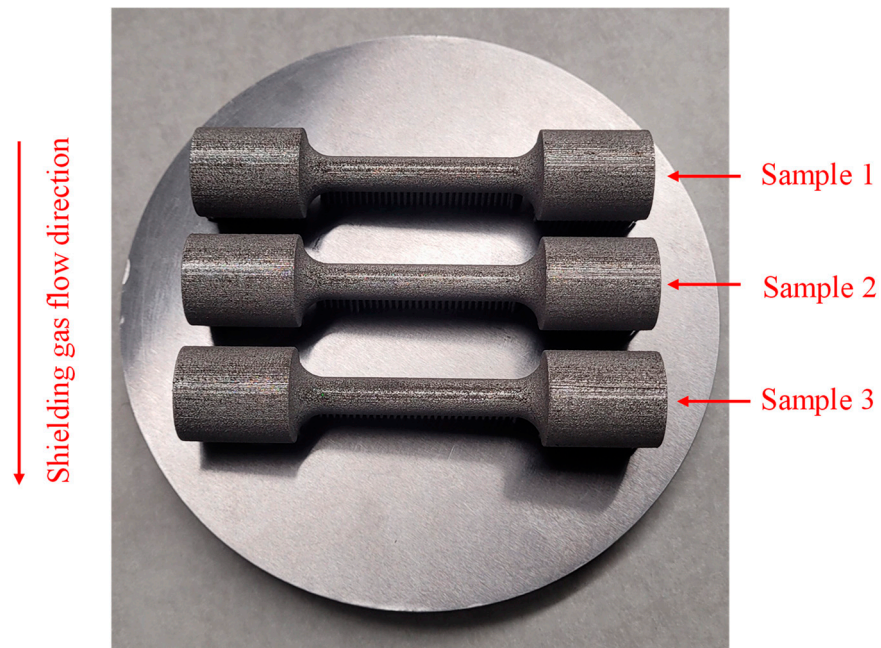


Figure 19. Printed tensile samples.

Table 9. Tensile test results of LPBF printed samples using the optimized parameters.

Sample	1	2	3
Yield strength (MPa)	1254.50	1131.70	960.10
Ultimate tensile strength (MPa)	1403.10	1366.70	1000.30
Elongation (%)	10.2	13.0	6.0

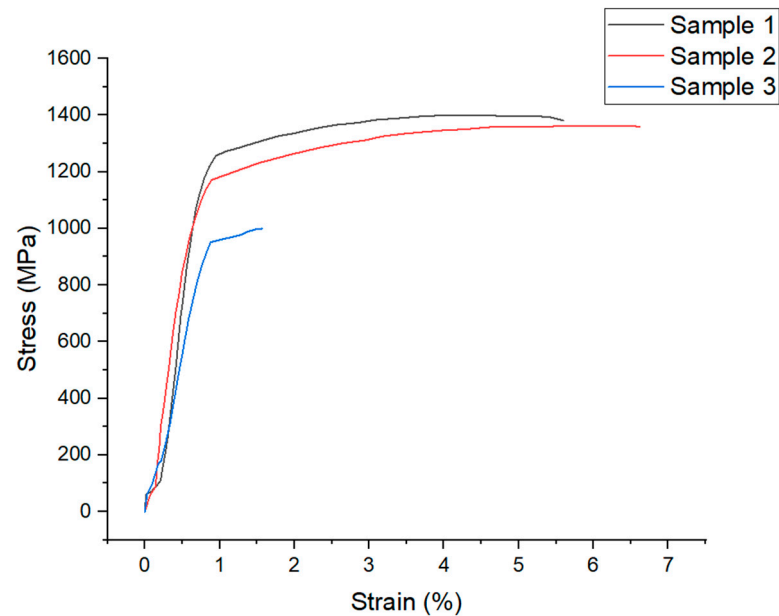


Figure 20. Tensile stress-strain curves.

Table 10 compares the average 2507 SDSS tensile properties of the printed three samples to the DIN EN 10088-3 standard. The LPBF samples showed higher UTS of  $1256.7 \pm 181.9$  MPa, and lower elongation of  $10.7 \pm 1.7\%$ . This behavior can be attributed to the higher ferritic microstructure of 89.3%. Kunz et al. [37] reported a similar mechanical behavior of LPBF printed samples with UTS and elongation of 1031 MPa and 14%,

respectively. They attributed this behavior to the resulting high ferritic microstructure of LPBF printed samples. Moreover, their heat-treated samples showed an increase in the austenite formation leading to a reduction in tensile strength and an increase in elongation (i.e., meeting the minimum requirements of the DIN EN 10088-3 standard).

**Table 10.** 2507 SDSS tensile properties for LPBF samples and DIN EN 10088-3 standard.

Material	Condition	Number of Samples	Yield Strength (MPa)	UTS (MPa)	Elongation (%)
2507 SDSS	DIN EN 10088-3 standard	-	>500	700–900	>25
	LPBF	3	1115.4 ± 120.7	1256.7 ± 181.9	10.7 ± 1.7

#### 4. Conclusions

In this study, the LPBF printing parameters, namely: laser power, scan speed, and hatch distance—were optimized to print highly dense 2507 super duplex stainless steel samples. A detailed design of the experiment using the RSM was conducted to investigate the various pore formation types along a wide energy density range (22.22–428.87 J/mm<sup>3</sup>), analyze the influence of each process parameter and their interactions on the resulting porosity, and find an optimal parameter set capable of producing highly dense printed parts. Moreover, an investigation was conducted on the microstructure and tensile properties of printed samples using the selected optimized parameter set. The following is a summary of the study's key findings:

- (1) Being the most prevalent pore types associated with the printing process parameters—the lack-of-fusion, gas or metallurgical, and keyhole pore regimes were identified for 2507 SDSS at energy density ranges from 22.22 J/mm<sup>3</sup> to 68.24 J/mm<sup>3</sup>, 68.24 J/mm<sup>3</sup> to 126.67 J/mm<sup>3</sup>, and 126.67 J/mm<sup>3</sup> to 428.87 J/mm<sup>3</sup>, respectively, with corresponding porosity ranges from 45.60% to 4.61%, 0.33% to 0.04%, and 0.15% to 1.56%.
- (2) A sharp decrease in the lack-of-fusion porosity is observed at low energy densities, where increasing the energy density from 22.22 J/mm<sup>3</sup> to 68.24 J/mm<sup>3</sup> resulted in a porosity decrease from 45.60% to 0.33%. Conversely, a gradual increase in the keyhole porosity from 0.15% to 1.56% is observed at higher energy densities from 126.67 J/mm<sup>3</sup> to 428.87 J/mm<sup>3</sup>, respectively.
- (3) The sample's position from the shielding gas and coater sweep directions can influence the resulting sample porosity. Positioning the samples far from both directions can adversely influence the sample's density. However, the position influence seems to be more significant from the shielding gas than the coater sweep.
- (4) The lack-of-fusion pores are relatively larger in size than the gas/metallurgical and keyhole pores, with mean ferret diameters of 0.26 mm, 0.05 mm, and 0.09 mm, respectively. Moreover, regarding the pore shape, the lack-of-fusion pores were observed to be irregular, with a mean aspect ratio of 0.33. Although the gas/metallurgical and keyhole pores showed roundish shapes. However, the gas/metallurgical pores were observed to be more spherical than keyhole pores, with, respectively, mean aspect ratios of 0.65 and 0.57.
- (5) A quadratic regression model between the input factors and the resulting porosity has been developed using the RSM. Model adequacy and accuracy checking has been conducted which indicated that the model satisfies the residual normality and constant variance assumptions with an RMSE and MAE of 4.735% and 3.917%, respectively.
- (6) The ANOVA analysis results showed that the linear terms of laser power, scan speed, and hatch distance were statistically significant, with *p*-values of 0.001, 0.001, and 0.004, respectively. However, the input factor non-linear effects were only observed to be significant for the laser power with a *p*-value of 0.003. Moreover, the factor interaction influence on the porosity was only observed to be significant for speed and hatch factors with a *p*-value of 0.011.

- (7) The influence of each input parameter on the porosity was investigated using 3D surface and contour plots. Regarding power vs. speed plots, it was observed that low laser powers coupled with high scan speeds resulted in a high porosity profile. Although a reduction in the porosity is seen with increasing the laser power while decreasing the scan speed; however, extreme high laser powers coupled with low scan speeds were observed to increase the porosity due to the formation of keyhole pores at higher energy densities.
- (8) The power vs. hatch plots showed that high porosities are present when having a combination of low laser power and high hatch distance. Moreover, it was observed that higher hatch distances should be avoided to prevent insufficient laser overlap leading to poor melting of the powder.
- (9) The speed vs. hatch plots indicated that higher porosities are seen when having higher scan speeds coupled with high hatch distances. Although decreasing the scan speed and hatch distance results in a reduction in the porosity; however, setting extremely low scan speeds and hatching distances is observed to increase the porosity, which is attributed to the resulting high energy densities.
- (10) The optimized parameters for laser power, scan speed, and hatch distance were 217.4 W, 1735.7 mm/s, and 51.3  $\mu\text{m}$ , respectively, which were able to print samples with a relative density of 99.961%.
- (11) Using the optimized parameter set, the as-built 2507 SDSS sample had a ferrite phase fraction of 89.3% with a yield and ultimate tensile strength of  $1115.4 \pm 120.7$  MPa and  $1256.7 \pm 181.9$  MPa, respectively.

**Author Contributions:** Conceptualization, A.J.Q. and A.M.; methodology, A.J.Q. and A.M.; software, A.M.; validation, A.M. and A.J.Q.; formal analysis, A.M.; investigation, A.M.; resources, A.J.Q.; data curation, A.M.; writing—original draft preparation, A.M.; writing—review and editing, A.M., A.J.Q. and S.D.; visualization, A.M.; supervision, A.J.Q., P.W. and S.D.; project administration, A.J.Q.; funding acquisition, A.J.Q. All authors have read and agreed to the published version of the manuscript.

**Funding:** This research was funded by Natural Sciences and Engineering Research Council of Canada (NSERC) grant number RGPIN-2016-04689 and Future Energy Systems (FES) grant number FES-T06-Q05 is highly appreciated.

**Data Availability Statement:** Not available.

**Conflicts of Interest:** The authors declare no conflict of interest. The authors declare that they have no known competing financial interests or personal relationships that could have appeared to influence the work reported in this paper.

## References

1. Tan, J.H.; Wong, W.L.E.; Dalgarno, K.W. An overview of powder granulometry on feedstock and part performance in the selective laser melting process. *Addit. Manuf.* **2017**, *18*, 228–255. [\[CrossRef\]](#)
2. DebRoy, T.; Wei, H.L.; Zuback, J.S.; Mukherjee, T.; Elmer, J.W.; Milewski, J.O.; Beese, A.M.; Wilson-Heid, A.; De, A.; Zhang, W. Additive manufacturing of metallic components—Process, structure and properties. *Prog. Mater. Sci.* **2018**, *92*, 112–224. [\[CrossRef\]](#)
3. Gu, D.D.; Meiners, W.; Wissenbach, K.; Poprawe, R. Laser additive manufacturing of metallic components: Materials, processes and mechanisms. *Int. Mater. Rev.* **2012**, *57*, 133–164. [\[CrossRef\]](#)
4. Herzog, D.; Seyda, V.; Wycisk, E.; Emmelmann, C. Additive manufacturing of metals. *Acta Mater.* **2016**, *117*, 371–392. [\[CrossRef\]](#)
5. Bourell, D.; Kruth, J.P.; Leu, M.; Levy, G.; Rosen, D.; Beese, A.M.; Clare, A. Materials for additive manufacturing. *CIRP Ann.* **2017**, *66*, 659–681. [\[CrossRef\]](#)
6. Schmidt, M.; Merklein, M.; Bourell, D.; Dimitrov, D.; Hausotte, T.; Wegener, K.; Overmeyer, L.; Vollertsen, F.; Levy, G.N. Laser based additive manufacturing in industry and academia. *CIRP Ann.* **2017**, *66*, 561–583. [\[CrossRef\]](#)
7. Afazov, S.; Denmark, W.A.; Toralles, B.L.; Holloway, A.; Yaghi, A. Distortion prediction and compensation in selective laser melting. *Addit. Manuf.* **2017**, *17*, 15–22. [\[CrossRef\]](#)
8. Yap, C.Y.; Chua, C.K.; Dong, Z.L.; Liu, Z.H.; Zhang, D.Q.; Loh, L.E.; Sing, S.L. Review of selective laser melting: Materials and applications. *Appl. Phys. Rev.* **2015**, *2*, 041101. [\[CrossRef\]](#)
9. Andani, M.T.; Dehghani, R.; Karamooz-Ravari, M.R.; Mirzaeifar, R.; Ni, J. A study on the effect of energy input on spatter particles creation during selective laser melting process. *Addit. Manuf.* **2018**, *20*, 33–43. [\[CrossRef\]](#)

10. Slotwinski, J.A.; Garboczi, E.J.; Stutzman, P.E.; Ferraris, C.F.; Watson, S.S.; Peltz, M.A. Characterization of Metal Powders Used for Additive Manufacturing. *J. Res. Natl. Inst. Stand. Technol.* **2014**, *119*, 460–493. [[CrossRef](#)]
11. Qu, S.; Ding, J.; Song, X. Achieving Triply Periodic Minimal Surface Thin-Walled Structures by Micro Laser Powder Bed Fusion Process. *Micromachines* **2021**, *12*, 705. [[CrossRef](#)]
12. Kempen, K. Expanding the Materials Palette for Selective Laser Melting of Metals. 2015. Available online: <https://lirias.kuleuven.be/1673720?limo=0> (accessed on 10 August 2022).
13. Zhang, B.; Li, Y.; Bai, Q. Defect Formation Mechanisms in Selective Laser Melting: A Review. *Chin. J. Mech. Eng.* **2017**, *30*, 515–527. [[CrossRef](#)]
14. Gong, H.; Rafi, K.; Gu, H.; Starr, T.; Stucker, B. Analysis of defect generation in Ti-6Al-4V parts made using powder bed fusion additive manufacturing processes. *Addit. Manuf.* **2014**, *1*, 87–98. [[CrossRef](#)]
15. Liu, J.; Wen, P. Metal vaporization and its influence during laser powder bed fusion process. *Mater. Des.* **2022**, *215*, 110505. [[CrossRef](#)]
16. Tang, M.; Pistorius, P.C.; Beuth, J.L. Prediction of lack-of-fusion porosity for powder bed fusion. *Addit. Manuf.* **2017**, *14*, 39–48. [[CrossRef](#)]
17. Cunningham, R.; Narra, S.P.; Ozturk, T.; Beuth, J.; Rollett, A.D. Evaluating the Effect of Processing Parameters on Porosity in Electron Beam Melted Ti-6Al-4V via Synchrotron X-ray Microtomography. *JOM* **2016**, *68*, 765–771. [[CrossRef](#)]
18. Cunningham, R.; Narra, S.P.; Montgomery, C.; Beuth, J.; Rollett, A.D. Synchrotron-Based X-ray Microtomography Characterization of the Effect of Processing Variables on Porosity Formation in Laser Powder-Bed Additive Manufacturing of Ti-6Al-4V. *JOM* **2017**, *69*, 479–484. [[CrossRef](#)]
19. du Plessis, A.; Yadroitsev, I.; Yadroitsava, I.; Le Roux, S.G. X-Ray Microcomputed Tomography in Additive Manufacturing: A Review of the Current Technology and Applications. *3D Print. Addit. Manuf.* **2018**, *5*, 227–247. [[CrossRef](#)]
20. Zhao, C.; Fezzaa, K.; Cunningham, R.W.; Wen, H.; De Carlo, F.; Chen, L.; Rollett, A.D.; Sun, T. Real-time monitoring of laser powder bed fusion process using high-speed X-ray imaging and diffraction. *Sci. Rep.* **2017**, *7*, 3602. [[CrossRef](#)]
21. Leung, C.L.A.; Marussi, S.; Atwood, R.C.; Towrie, M.; Withers, P.J.; Lee, P.D. In situ X-ray imaging of defect and molten pool dynamics in laser additive manufacturing. *Nat. Commun.* **2018**, *9*, 1355. [[CrossRef](#)]
22. Cunningham, R.; Zhao, C.; Parab, N.; Kantzos, C.; Pauza, J.; Fezzaa, K.; Sun, T.; Rollett, A.D. Keyhole threshold and morphology in laser melting revealed by ultrahigh-speed x-ray imaging. *Science* **2019**, *363*, 849–852. [[CrossRef](#)] [[PubMed](#)]
23. du Plessis, A. Effects of process parameters on porosity in laser powder bed fusion revealed by X-ray tomography. *Addit. Manuf.* **2019**, *30*, 100871. [[CrossRef](#)]
24. Ter Haar, G.M.; Becker, T.H. Selective Laser Melting Produced Ti-6Al-4V: Post-Process Heat Treatments to Achieve Superior Tensile Properties. *Materials* **2018**, *11*, 146. [[CrossRef](#)] [[PubMed](#)]
25. Suryawanshi, J.; Prashanth, K.G.; Scudino, S.; Eckert, J.; Prakash, O.; Ramamurty, U. Simultaneous enhancements of strength and toughness in an Al-12Si alloy synthesized using selective laser melting. *Acta Mater.* **2016**, *115*, 285–294. [[CrossRef](#)]
26. Iturrioz, A.; Gil, E.; Petite, M.M.; Garcandia, F.; Mancisidor, A.M.; Sebastian, M.S. Selective laser melting of AlSi10Mg alloy: Influence of heat treatment condition on mechanical properties and microstructure. *Weld. World* **2018**, *62*, 885–892. [[CrossRef](#)]
27. Spierings, A.; Dawson, K.; Kern, K.; Palm, F.; Wegener, K. SLM-processed Sc- and Zr- modified Al-Mg alloy: Mechanical properties and microstructural effects of heat treatment. *Mater. Sci. Eng. A* **2017**, *701*, 264–273. [[CrossRef](#)]
28. Takaichi, A.; Suyalatu; Nakamoto, T.; Joko, N.; Nomura, N.; Tsutsumi, Y.; Migita, S.; Doi, H.; Kurosu, S.; Chiba, A.; et al. Microstructures and mechanical properties of Co-29Cr-6Mo alloy fabricated by selective laser melting process for dental applications. *J. Mech. Behav. Biomed. Mater.* **2013**, *21*, 67–76. [[CrossRef](#)] [[PubMed](#)]
29. Tomus, D.; Rometsch, P.A.; Heilmaier, M.; Wu, X. Effect of minor alloying elements on crack-formation characteristics of Hastelloy-X manufactured by selective laser melting. *Addit. Manuf.* **2017**, *16*, 65–72. [[CrossRef](#)]
30. Deng, D.; Peng, R.L.; Brodin, H.; Moverare, J. Microstructure and mechanical properties of Inconel 718 produced by selective laser melting: Sample orientation dependence and effects of post heat treatments. *Mater. Sci. Eng. A* **2018**, *713*, 294–306. [[CrossRef](#)]
31. Choo, H.; Sham, K.-L.; Bohling, J.; Ngo, A.; Xiao, X.; Ren, Y.; Depond, P.J.; Matthews, M.J.; Garlea, E. Effect of laser power on defect, texture, and microstructure of a laser powder bed fusion processed 316L stainless steel. *Mater. Des.* **2018**, *164*, 107534. [[CrossRef](#)]
32. Yang, K.-T.; Kim, M.-K.; Kim, D.; Suhr, J. Investigation of laser powder bed fusion manufacturing and post-processing for surface quality of as-built 17-4PH stainless steel. *Surf. Coat. Technol.* **2021**, *422*, 127492. [[CrossRef](#)]
33. Zhang, Z.; Zhang, H.; Hu, J.; Qi, X.; Bian, Y.; Shen, A.; Xu, P.; Zhao, Y. Microstructure evolution and mechanical properties of briefly heat-treated SAF 2507 super duplex stainless steel welds. *Constr. Build. Mater.* **2018**, *168*, 338–345. [[CrossRef](#)]
34. Martins, M.; Casteletti, L.C. Heat treatment temperature influence on ASTM A890 GR 6A super duplex stainless steel microstructure. *Mater. Charact.* **2005**, *55*, 225–233. [[CrossRef](#)]
35. Davidson, K.; Singamneni, S. Selective Laser Melting of Duplex Stainless Steel Powders: An Investigation. *Mater. Manuf. Process.* **2016**, *31*, 1543–1555. [[CrossRef](#)]
36. Saeidi, K.; Kevetkova, L.; Lofaj, F.; Shen, Z. Novel ferritic stainless steel formed by laser melting from duplex stainless steel powder with advanced mechanical properties and high ductility. *Mater. Sci. Eng. A* **2016**, *665*, 59–65. [[CrossRef](#)]

37. Kunz, J.; Boontanom, A.; Herzog, S.; Suwanpinij, P.; Kaletsch, A.; Broeckmann, C. Influence of hot isostatic pressing post-treatment on the microstructure and mechanical behavior of standard and super duplex stainless steel produced by laser powder bed fusion. *Mater. Sci. Eng. A* **2020**, *794*, 139806. [[CrossRef](#)]
38. Wang, G.; Huang, L.; Liu, Z.; Qin, Z.; He, W.; Liu, F.; Chen, C.; Nie, Y. Process optimization and mechanical properties of oxide dispersion strengthened nickel-based superalloy by selective laser melting. *Mater. Des.* **2019**, *188*, 108418. [[CrossRef](#)]
39. Ternner, M.; Ricordel, T.; Cho, J.-H.; Lee, J.-S. The Response Surface Methodology for Optimizing the Process Parameters of Selective Laser Melting. *J. Weld. Join.* **2019**, *37*, 27–39. [[CrossRef](#)]
40. Deng, Y.; Mao, Z.; Yang, N.; Niu, X.; Lu, X. Collaborative Optimization of Density and Surface Roughness of 316L Stainless Steel in Selective Laser Melting. *Materials* **2020**, *13*, 1601. [[CrossRef](#)]
41. Montgomery, D.C. *Design and Analysis of Experiments*, 8th ed.; Arizona State University: Tempe, AZ, USA, 2013.
42. Hyer, H.C.; Petrie, C.M. Effect of powder layer thickness on the microstructural development of additively manufactured SS316. *J. Manuf. Process.* **2022**, *76*, 666–674. [[CrossRef](#)]
43. Ferrar, B.; Mullen, L.; Jones, E.; Stamp, R.; Sutcliffe, C.J. Gas flow effects on selective laser melting (SLM) manufacturing performance. *J. Mater. Process. Technol.* **2012**, *212*, 355–364. [[CrossRef](#)]
44. Hosseini, V.A.; Wessman, S.; Hurtig, K.; Karlsson, L. Nitrogen loss and effects on microstructure in multipass TIG welding of a super duplex stainless steel. *Mater. Des.* **2016**, *98*, 88–97. [[CrossRef](#)]
45. Haghdadi, N.; Laleh, M.; Chen, H.; Chen, Z.; Ledermueller, C.; Liao, X.; Ringer, S.; Primig, S. On the pitting corrosion of 2205 duplex stainless steel produced by laser powder bed fusion additive manufacturing in the as-built and post-processed conditions. *Mater. Des.* **2021**, *212*, 110260. [[CrossRef](#)]
46. Nigon, G.N.; Isgor, O.B.; Pasebani, S. The effect of annealing on the selective laser melting of 2205 duplex stainless steel: Microstructure, grain orientation, and manufacturing challenges. *Opt. Laser Technol.* **2020**, *134*, 106643. [[CrossRef](#)]

**Disclaimer/Publisher's Note:** The statements, opinions and data contained in all publications are solely those of the individual author(s) and contributor(s) and not of MDPI and/or the editor(s). MDPI and/or the editor(s) disclaim responsibility for any injury to people or property resulting from any ideas, methods, instructions or products referred to in the content.